



저작자표시-비영리-변경금지 2.0 대한민국

이용자는 아래의 조건을 따르는 경우에 한하여 자유롭게

- 이 저작물을 복제, 배포, 전송, 전시, 공연 및 방송할 수 있습니다.

다음과 같은 조건을 따라야 합니다:



저작자표시. 귀하는 원저작자를 표시하여야 합니다.



비영리. 귀하는 이 저작물을 영리 목적으로 이용할 수 없습니다.



변경금지. 귀하는 이 저작물을 개작, 변형 또는 가공할 수 없습니다.

- 귀하는, 이 저작물의 재이용이나 배포의 경우, 이 저작물에 적용된 이용허락조건을 명확하게 나타내어야 합니다.
- 저작권자로부터 별도의 허가를 받으면 이러한 조건들은 적용되지 않습니다.

저작권법에 따른 이용자의 권리는 위의 내용에 의하여 영향을 받지 않습니다.

이것은 [이용허락규약\(Legal Code\)](#)을 이해하기 쉽게 요약한 것입니다.

[Disclaimer](#)

Thesis for the Degree of Master of Engineering

Luminescence Properties of Gadolinium Strontium
Aluminate Phosphor and Luminescence Enhancement
by Co-doping Lithium Ion for White LEDs

by

Woo Tae Hong

Department of LED Convergence Engineering
Specialized Graduate School Science & Technology
Convergence

Pukyong National University

February 2016

Luminescence Properties of Gadolinium Strontium
Aluminate Phosphor and Luminescence Enhancement
by Co-doping Lithium Ion for White LEDs
(백색 LED 응용을 위한 Gadolinium Strontium
Aluminate계 형광체의 형광특성 및 Lithium ion
도핑에 따른 형광효율의 농도 의존성 연구)

Advisor: Prof. Hyun Kyoung Yang

by
Woo Tae Hong

A thesis submitted in partial fulfillment of the requirements
for the degree of

Master of Engineering

in Department of LED Convergence Engineering
Specialized Graduate School Science & Technology Convergence,
Pukyong National University

February 2016

Luminescence Properties of Gadolinium Strontium Aluminate
Phosphor and Luminescence Enhancement by Co-doping
Lithium Ion for White LEDs

A dissertation

by

Woo Tae Hong

Approved by:

(Chairman) Jung Hyun Jeong

(Member) Ganji Seeta Rama Raju

(Member) Hyun Kyoung Yang

February 26, 2016

List

Abstract.....	vii
1. Introduction.....	1
2. Theoretical backgrounds.....	5
2. 1 Phosphor.....	5
2. 1. 1 Luminescent material.....	5
2. 1. 2 Luminescent mechanism.....	8
2. 1. 3 Applications of phosphors	11
2. 1. 4 Phosphors based light emitting diode	13
2. 2 Structure of $\text{GdSr}_2\text{AlO}_5$	16
2. 3 The luminescence properties of Ce^{3+} in phosphor.....	18
2. 4 The effect of the Li^+ co-doping in phosphor	20
3. Experimental	22
3. 1 Preparation of samples	22
3. 1. 1 Preparation of $\text{Gd}_{1-x}\text{Sr}_2\text{AlO}_5:x\text{Ce}^{3+}$ (GSA: Ce^{3+}) using a high-energy ball milling.....	23
3. 1. 2 Preparation of $(\text{Gd}_{0.98}\text{Ce}_{0.02})\text{Sr}_2\text{AlO}_5:x\text{Li}^+$ (GSA: Ce^{3+} , Li^+) using a high-energy ball milling	24
3. 1. 3 Preparation of $(\text{Gd}_{0.95}\text{Ce}_{0.05})\text{Sr}_2\text{AlO}_5:x\text{Li}^+$ (GSA: Ce^{3+} , Li^+) using a	

sol-gel method	25
3. 2 High-energy ball milling process	26
3. 3 Sol-gel method	28
3. 4 Characterizations of the phosphors.....	30
4. Result and discussion.....	34
4. 1 $Gd_{1-x}Sr_2AlO_5:xCe^{3+}$ prepared by high-energy ball milling.....	34
4. 2 $(Gd_{0.98}Ce_{0.02})Sr_2AlO_5:xLi^+$ prepared by high-energy ball milling	45
4. 3 $(Gd_{0.95}Ce_{0.05})Sr_2AlO_5:xLi^+$ prepared by sol-gel method	58
5. Conclusion	68
References.....	71

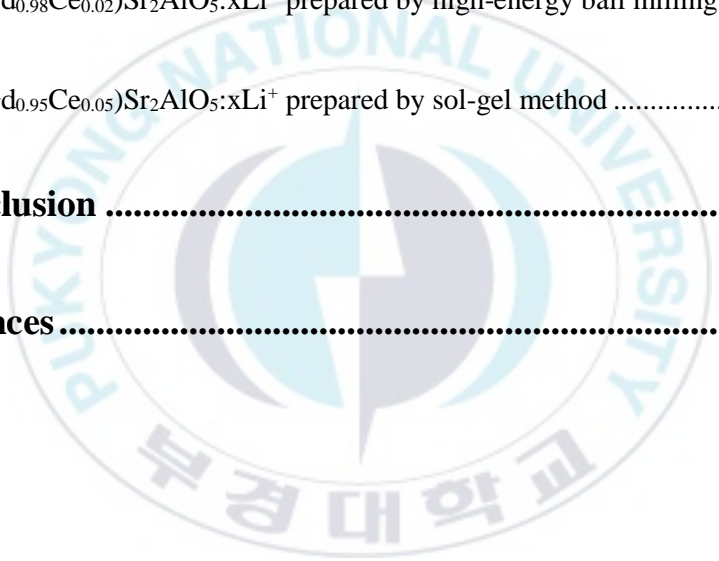


Table List

Table 2. 1 Phosphor device.....	12
Table 4. 1 CIE 1931 color coordinate and color temperature of YAG:Ce ³⁺ phosphors and GSA:Ce ³⁺ (Gd _{0.98} Sr ₂ AlO ₅ :0.02Ce ³⁺) phosphors encapsulated white LEDs, respectively.....	44
Table 4. 2 CIE 1931 color coordinate and color temperature of GSA:Ce ³⁺ (Gd _{0.98} Ce _{0.02} Sr ₂ AlO ₅) phosphors and GSA:Ce ³⁺ , Li ⁺ (Gd _{0.98} Ce _{0.02} Sr ₂ AlO ₅ :0.10Li ⁺) phosphors encapsulated white LEDs, respectively.....	57

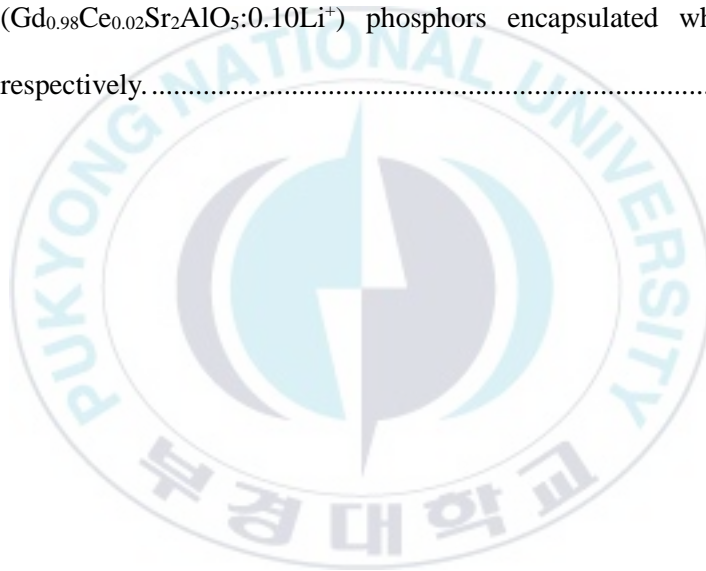


Figure List

Figure 2. 1 Schematic diagram of luminescent mechanism in phosphor.	8
Figure 2. 2 Crystal structure of $\text{GdSr}_2\text{AlO}_5:\text{Ce}^{3+}$	16
Figure 2. 3 Energy band of free Ce^{3+} ion and crystal field splitting that is occurred by host lattice.....	18
Figure 3. 1 Schematic diagram of processing steps involved in synthesis of $\text{GdSr}_2\text{AlO}_5:\text{Ce}^{3+}$ powder phosphors.....	22
Figure 3. 2 Planetary ball milling machine “Pulverisette 5” and its working mechanism.	27
Figure 3. 3 Schematic representation of the sol-gel method.	29
Figure 3. 4 Thermo Gravimetric - Differential Thermal Analyzer (Perkin Elmer TGA7-DTA7).....	31
Figure 3. 5 X-ray diffractometer (Philips X’Pert/MPD).	32
Figure 3. 6 Time resolved spectrometer system (PTI).	32
Figure 3. 7 Field emission scanning electron microscope (JEOL, JSM-6700F).	33
Figure 4. 1 TG/DTA curves of $\text{GSA}:\text{Ce}^{3+}$ powder precursor in air.....	34
Figure 4. 2 X-ray diffraction patterns of $\text{GSA}:\text{Ce}^{3+}$ for different Ce^{3+} concentration.	35
Figure 4. 3 FE-SEM image of $\text{Gd}_{0.98}\text{Sr}_2\text{AlO}_5:0.02\text{Ce}^{3+}$ phosphor.....	36
Figure 4. 4 (a) PLE spectra ($\lambda_{\text{em}} = 576 \text{ nm}$) of $\text{GSA}:\text{Ce}^{3+}$ phosphor for different Ce^{3+} ion concentration and (b) Gaussian function fitting graph of PLE spectra for $\text{Gd}_{0.98}\text{Sr}_2\text{AlO}_5:0.02\text{Ce}^{3+}$ phosphor.....	37
Figure 4. 5 (a) PL spectra ($\lambda_{\text{ex}} = 438 \text{ nm}$) and (b) maximum PL and PLE intensity of $\text{GSA}:\text{Ce}^{3+}$ phosphors as a function of Ce^{3+} ion concentration.....	39

Figure 4. 6 (a) Gaussian function fitting graph of PL spectra for $\text{Gd}_{0.98}\text{Sr}_2\text{AlO}_5:0.02\text{Ce}^{3+}$ phosphor and (b) Gaussian function peak as a function of Ce^{3+} ion concentration.....	41
Figure 4. 7 (a) Emission spectra of fabricated white LEDs (blue LED chip + $\text{Gd}_{0.98}\text{Sr}_2\text{AlO}_5:0.02\text{Ce}^{3+}$ phosphor), (b) CIE 1931 color coordinate of fabricated white LEDs and commercial white LEDs (blue LED chip + YAG:Ce phosphors).....	43
Figure 4. 8 TG/DTA curves of GSA: Ce^{3+} , Li^+ phosphors where (a) $x = 0$ and (b) $x = 0.10$	45
Figure 4. 9 X-ray diffraction patterns of GSA: Ce^{3+} , Li^+ for different Li^+ concentration.....	46
Figure 4. 10 FE-SEM images of GSA: Ce^{3+} , Li^+ phosphors where (a) $x = 0$ and (b) $x = 0.10$	48
Figure 4. 11 (a) PLE spectra ($\lambda_{\text{em}} = 574 \text{ nm}$) of GSA: Ce^{3+} , Li^+ phosphor for different Li^+ ion concentration and (b) Gaussian function fitting graph of PLE spectra for $\text{Gd}_{0.98}\text{Ce}_{0.02}\text{Sr}_2\text{AlO}_5:0.10\text{Li}^+$ phosphor. ...	49
Figure 4. 12 (a) PL spectra ($\lambda_{\text{ex}} = 437 \text{ nm}$) and (b) maximum PL and PLE intensity of GSA: Ce^{3+} , Li^+ phosphors as a function of Li^+ ion concentration.....	51
Figure 4. 13 (a) Gaussian function fitting graph of PL spectra for $\text{Gd}_{0.98}\text{Ce}_{0.02}\text{Sr}_2\text{AlO}_5:0.10\text{Li}^+$ phosphor and (b) Gaussian function peak as a function of Li^+ ion concentration.	53
Figure 4. 14 Schematic diagram of energy level alteration by Li^+ co-doping in GSA: Ce^{3+}	55
Figure 4. 15 Comparison of the (a) Emission spectra and (b) CIE 1931 color coordinate of fabricated white LEDs (blue LED chip + GSA: Ce^{3+} , blue LED chip + GSA: Ce^{3+} , Li^+ ; $x = 0.10$).....	56

Figure 4. 16 X-ray diffraction patterns of GSA:Ce ³⁺ , Li ⁺ phosphor for different Li ⁺ concentration.....	58
Figure 4. 17 FE-SEM images of Gd _{0.95} Ce _{0.05} Sr ₂ AlO ₅ :xLi ⁺ where (a) x = 0, (b) x = 0.025, (c) x = 0.050, (d) x = 0.100, (e) x = 0.150, (f) x = 0.200 and (g) x = 0.250.....	60
Figure 4. 18 (a) PLE spectra ($\lambda_{em} = 572$ nm) and (b) Gaussian function fitting graph of PLE spectra for Gd _{0.95} Ce _{0.05} Sr ₂ AlO ₅ :0.025Li ⁺ phosphor.	61
Figure 4. 19 (a) PL spectra ($\lambda_{ex} = 437$ nm), (b) Gaussian function fitting graph of PL spectra and (c) PL, PLE intensity graph of GSA:Ce ³⁺ , Li ⁺ phosphors as a function of Li ⁺ concentration.....	63
Figure 4. 20 Comparison of (a) PL spectra and (b) normalized PL spectra of GSA:Ce ³⁺ , Li ⁺ phosphor synthesized by high-energy ball milling and sol-gel method.....	65
Figure 4. 21 CIE color coordinate of GSA:Ce ³⁺ , Li ⁺ phosphor synthesized by high-energy ball milling (HEB) and sol-gel method.....	66

Luminescence properties of cerium doped gadolinium strontium
aluminate phosphor and luminescence enhancement by co-doping lithium
ion for white LEDs

Woo Tae Hong

Department of LED-marine convergence, Specialized Graduate School

Science & Technology Convergence

Pukyong National University

Abstract

A series of trivalent cerium (Ce^{3+}) ions doped gadolinium strontium aluminate ($\text{Gd}_{1-x}\text{Sr}_2\text{AlO}_5:x\text{Ce}^{3+}$ (GSA: Ce^{3+})) yellow phosphors were prepared by a high-energy ball milling process. The X-ray diffraction patterns confirmed the complex phase of GSA: Ce^{3+} phosphors with tetragonal structure of $\text{GdSr}_2\text{AlO}_5$ phase and GdSrAlO_4 phase. The photoluminescence excitation spectra exhibited the broad band with

dominant excitation wavelength of 438 nm due to 4f-5d transition of Ce^{3+} ion in GSA host lattice. The photoluminescence emission spectra under 438 nm excitation showed yellow emission corresponding to the 5d-4f transition of Ce^{3+} ion. Concentration quenching in the PL intensity was observed when the Ce^{3+} ion concentration was increased over 2 mol% ($x = 0.02$) in the GSA host lattice. The emission peak of $\text{GSA}:\text{Ce}^{3+}$ was shifted to the red region due to the enlargement of crystal splitting for Ce^{3+} ions. The white LEDs which were fabricated by blue LED (460 nm) chip and $\text{GSA}:\text{Ce}^{3+}$ phosphor unveiled the CIE 1931 chromaticity coordinates of (0.347, 0.311).

In order to improve the luminescence efficiency of $\text{GSA}:\text{Ce}^{3+}$ phosphor, Li^+ ions were doped into the $(\text{Gd}_{0.98}\text{Ce}_{0.02})\text{Sr}_2\text{AlO}_5$ ($\text{GSA}:\text{Ce}^{3+}, \text{Li}^+$) phosphors. The XRD patterns of the $\text{GSA}:\text{Ce}^{3+}, \text{Li}^+$ phosphors confirmed complex phase of with tetragonal structure of $\text{GdSr}_2\text{AlO}_5$ phase and GdSrAlO_4 phase. Compared with $\text{GSA}:\text{Ce}^{3+}$ phosphors, the yellow emission of $\text{GSA}:\text{Ce}^{3+}, \text{Li}^+$ was increased by a factor of 5.17 when doped with 10 mol% Li^+ ions due to the local crystal field distortion in $\text{GdSr}_2\text{AlO}_5:\text{Ce}^{3+}$ host lattice. White LEDs were fabricated by encapsulating the $\text{GSA}:\text{Ce}^{3+}, \text{Li}^+$ phosphors on blue LED chips. The enhancement of the yellow emission in $\text{GSA}:\text{Ce}^{3+}, \text{Li}^+$ phosphors induces the color rendering improvement of white LEDs

The GSA:Ce³⁺, Li⁺ phosphors were synthesized by using sol-gel method for different Li⁺ concentration. The XRD patterns of the GSA:Ce³⁺, Li⁺ phosphors synthesized by sol-gel method confirmed that the crystallinity of impurity decreased compared with the high-energy ball milling. The FE-SEM images confirm that the particles of phosphors grew and aggregated each other, when the Li⁺ concentration in GSA:Ce³⁺, Li⁺ phosphors increased. By adding 2.5 mol% of Li⁺ in GSA:Ce³⁺, the emission intensity of GSA:Ce³⁺, Li⁺ was increased to 1.7 times higher than GSA:Ce³⁺ phosphors. In terms of the synthesis method, emission intensity of the GSA:Ce³⁺, Li⁺ phosphors fabricated by sol-gel method was 3 times lower than the other phosphors. However, the color purity of the GSA:Ce³⁺, Li⁺ phosphors fabricated by sol-gel method is better than the other phosphors due to the low quantity of the impurity phase.

1. Introduction

Nowadays, the usage of light-emitting diodes (LEDs) improved gradually by replacing the incandescent lamps owing to their enhanced luminescence efficiency and environmental friendliness and long working lifetime [1-6]. Generally, the commercial white LEDs are fabricated by combining with blue InGaN LED chip and yellow emitting YAG:Ce³⁺ phosphors. These commercial white LEDs have various advantages such as high luminescence efficiency, good thermal stability at junction temperature of LED chip and low cost [7-9]. Despite of these benefits, the commercial white LEDs exhibits high correlated color temperature (CCT) and low color rendering index (CRI) due to the shortage of red emission [10, 11]. To overcome these shortcomings, the CRI has been improved by different approaches such as the combination of UV-LED with red/green/blue (RGB) phosphors [12-14], encapsulating a red emitting component in the commercial white LEDs [15-17] and/or by combining the blue LED chips with new yellow phosphors with enhanced red region [18-21].

The photoluminescence spectra of trivalent cerium ion (Ce³⁺ ion) usually shows a wide band due to the parity allowed characteristics of the 5d-4f transition between the lowest crystal field components (5d state) and its

ground states ($^2F_{7/2}$ and $^2F_{5/2}$), leading to the emission region from ultraviolet to yellow, depending on the kind of host lattices.

The Ce^{3+} ion doped gadolinium strontium aluminate ($GdSr_2AlO_5:Ce^{3+}$, GSA: Ce^{3+}) phosphors exhibits the broad luminescence in the yellow region with a band maximum of 565 nm when exciting with 442 nm radiation [22]. By focusing on these properties, GSA: Ce^{3+} phosphors may replace the YAG: Ce^{3+} phosphor to represent warm white light. Although GSA: Ce^{3+} phosphors have a potentiality to replace the YAG: Ce^{3+} phosphors, the luminescence efficiency was lower than that of YAG: Ce^{3+} phosphor, which make difficult to use GSA: Ce^{3+} phosphors instead of the YAG: Ce^{3+} phosphors.

In this work, our efforts have been focused to increase the luminescence intensity by controlling the luminescence properties of $GdSr_2AlO_5:Ce^{3+}$ compounds. Im *et al.* shown that the increased luminescence efficiency of the GSA: Ce^{3+} by the introduction of Sr^{2+} and F^- ions [23] or Si^{4+} ion [24] into the host lattice and controlled the dominant wavelength due to the variations in the crystal field environment of Ce^{3+} ion in the GSA host lattice. Also, doping of lanthanide or alkali-earth metal or boron group ions in GSA: Ce^{3+} compounds can control the luminescence properties and luminescence intensity [25, 26]. To the best of our knowledge, the Li^+ co-doping effect of GSA: Ce^{3+} phosphor has not been reported.

The effects of Li^+ ions co-doping have been studied in many phosphors. The Li^+ co-dopant reveals a superior effect on enhanced luminescence of Ce^{3+} or Eu^{2+} , which exhibits f-d transitions. The effect of Li^+ co-doping, several mechanisms were proposed, such as decreasing the Stokes shift [27], forming charge trap population [28], charge compensation [29], acting as a flux agent [30, 31], altering the crystal field [32] and increasing absorbance and re-absorbance [33].

In the $\text{GSA}:\text{Ce}^{3+}$ compounds [34], the unit cell of $\text{GSA}:\text{Ce}^{3+}$ consists of $(\text{Gd}, \text{Ce})\text{SrO}^{3+}$ layers and SrAlO_4^{3-} layers along the c -axis. The Gd^{3+} ion, Ce^{3+} ion and half Sr^{2+} ions share the $8h$ site in $(\text{Gd}, \text{Ce})\text{SrO}^{3+}$ layers. Two O^{2-} ion in the $4c$ site and six O^{2-} ions in the $16l$ site surround in Gd^{3+} , Ce^{3+} and half Sr^{2+} ion that coordinated in GdO_8 , CeO_8 , SrO_8 polyhedron. We expect that the Li^+ co-doping can affect the luminescence properties of $\text{GSA}:\text{Ce}^{3+}$ phosphors by optimizing crystal field of CeO_8 polyhedron.

In this thesis, we reported a series of Ce^{3+} ions doped $\text{Gd}_{1-x}\text{Sr}_2\text{AlO}_5:x\text{Ce}^{3+}$, ($\text{GSA}:\text{Ce}^{3+}$) and Li^+ ions co-doped $\text{GSA}:\text{Ce}^{3+}$ ($\text{GSA}:\text{Ce}^{3+}, \text{Li}^+$) phosphors by a high-energy ball milling method and a sol-gel method. The luminescence properties, crystal structure and surface morphology of the $\text{GSA}:\text{Ce}^{3+}$ and $\text{GSA}:\text{Ce}^{3+}, \text{Li}^+$ were studied. The synthesized phosphors were used to fabricate the WLED by combining with InGaN LED chip. The Commission Internationale de l'Eclairage (CIE) chromaticity coordinates

were calculated, and CRI properties were compared with commercial GSA:Ce-encapsulated LEDs.



2. Theoretical backgrounds

2. 1 Phosphor

The definition of the word ‘phosphor’ itself is not clearly defined and is dependent on the user. In narrow sense, the word is used to mean inorganic phosphor, usually those in powder form and synthesized for the purpose of practical applications. Single crystals, thin films and organic molecules that exhibit luminescence are rarely called phosphors. In a broad sense, the word ‘phosphor’ is equivalent to ‘solid luminescence material’.

2. 1. 1 Luminescent material

Luminescence materials also called a phosphor are a crystal compound which converts certain types of energy into electromagnetic radiation over and above thermal radiation. When you heat a solid to a temperature in excess of about 600 °C, it emits infrared radiation. This is thermal radiation (and not luminescence). The electromagnetic radiation emitted by a luminescent material is usually in the visible region, but can also be in other spectral regions, such as ultraviolet or infrared. Luminescence can be excited by many kinds of energy. Photoluminescence is excited by electromagnetic (often ultraviolet) radiation, cathodoluminescence is

excited by a beam of energetic electrons, electroluminescence is excited by an electric voltage, triboluminescence is excited by mechanical energy, X-ray luminescence is excited by X-ray, chemiluminescence is excited by the energy of a chemical reaction, and so on.

Note that thermoluminescence does not refer to thermal excitation, but to stimulation of luminescence which was excited by different way. In figure 1.1.2, we have drawn schematically a crystal or a grain of a photoluminescent material in order to illustrate the definition of luminescence. The system consists of a host lattice and a luminescent center which often so called an activator. For example, consider the famous luminescent materials, such as $\text{Y}_3\text{Al}_5\text{O}_{12}:\text{Ce}^{3+}$ and $\text{BaMgAl}_{10}\text{O}_{17}:\text{Eu}^{2+}$. The host lattice are $\text{Y}_3\text{Al}_5\text{O}_{12}$ and $\text{BaMgAl}_{10}\text{O}_{17}$, the activators are the Ce^{3+} and Eu^{2+} ions. The luminescence processes in such a system are as follows. The exciting radiation is absorbed by the host material, and host material is excited activator, which then raises it to an excited state. And then it returns to the ground state by an emission of radiation (a photon). Competing with this process, there exists lattice vibrations, or phonons, to heat the host lattice. The host lattice does not participate in the optical processes, but simply “holds” the activator ion while the activator ions absorb the energy and emit optical radiation. Another luminescence process is one in which another ion is absorb exciting radiation and then transfers this excitation

energy to the activator ions. In this case, absorbing ion is called a sensitizer. One example is $\text{YVO}_4:\text{Eu}^{3+}, \text{Bi}^{3+}$ in which Bi^{3+} ions absorbs ultraviolet (exciting) radiation and then excitation energy is transferred from Bi^{3+} to Eu^{3+} . The emission consists partly of Bi^{3+} emission and partly of Eu^{3+} emission.



2. 1. 2 Luminescent mechanism

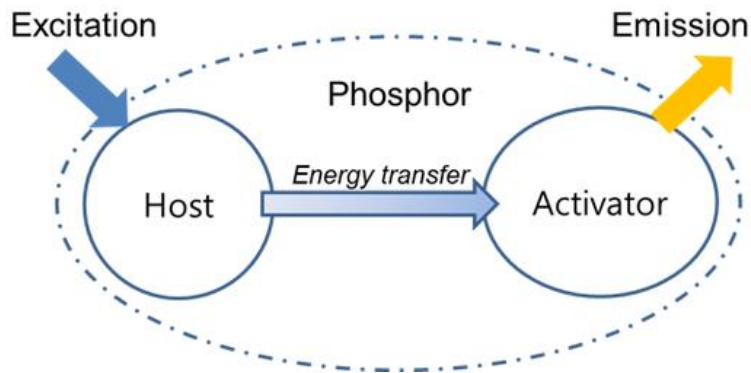


Figure 2. 1 Schematic diagram of luminescent mechanism in phosphor.

Luminescent materials are mostly solid inorganic materials consisting of a host lattice, usually intentionally doped with impurities, shown in Figure 2.1. The impurity concentrations generally are low in view of the fact that at higher concentrations the efficiency of the luminescence process usually decreases (concentration quenching, see below). In addition, most of the phosphors have a white body color.

Especially for fluorescent lamps, this is an essential feature to prevent absorption of visible light by the phosphors used. The absorption of energy, which is used to excite the luminescence, takes place by either the host lattice or intentionally doped impurities. In most cases, the emission takes place on the impurity ions, which, when they also generate the desired emission, are called activator ions. When the activator ions show too weak an absorption, a second kind of impurities can be added (sensitizers), which absorb the energy and subsequently transfer the energy to the activators.

This process involves transport of energy through the luminescent materials. Quite frequently, the emission color can be adjusted by choosing the proper impurity ion, without changing the host lattice in which the impurity ions are incorporated. On the other hand, quite a few activator ions show emission spectra with emission at spectral positions which are hardly influenced by their chemical environment. This is especially true for many of the rare-earth ions. Energy transfer between a sensitizer ion (S) and an activator ion (A) can be written as a chemical reaction: $S^* + A \rightarrow S + A^*$, where the asterisk indicates the excited state. In the phosphor, the symmetrical stretching is a vibration mode in which the central metal ion is at rest and the surrounding ligands are moving in phase away from the metal ion and coming back. Therefore, configurational coordinate diagram is described as the potential energy curves of the absorbing center as a function of a configurational coordinate that means one of the vibration modes of the center as shown in Figure 2.2. Stokes shift is defined as the energy difference between the excitation maximum and emission maximum of the lowest excitation band and that of the emission band. The Stokes shift (ΔR) can be calculated as follows.

$$\text{Stoke shift} = 2S \cdot \omega_m$$

where, ω_m and S are the mean phonon frequency and Huang-Rhys factor, respectively. The value of S is the strength of the electron lattice coupling,

which is proportional to $(\Delta R)^2$ [35]. As shown in Figure 2.3, the probability for the transition from ground states to excited states is highest at $R = R_0$. If the transitions take place, at $R < R_0$: less probable, larger energy difference ($E_0 + \Delta E_1$) and at $R > R_0$; less probable, smaller energy difference ($E_0 - \Delta E_2$). Because the probability for the transition is related to the intensity of absorption, the peak with the strongest intensity is at R_0 (corresponding to E_0) and has the broadness [36].



2. 1. 3 Applications of phosphors

The applications of phosphors can be classified as:

- (1) light sources represented by fluorescent lamps;
- (2) display devices represented by cathode-ray tubes;
- (3) detector systems represented by X-ray screens and scintillators;
- (4) other simple applications, such as luminous paint with long persistent phosphorescence.

Another method to classify the applications is according to the excitation source for the phosphors. Table 1 lists various kinds of phosphor devices according to the method used to excite the phosphor. It gives a summary of phosphor devices by the manner in which the phosphors are applied. No further explanation of the table is necessary.

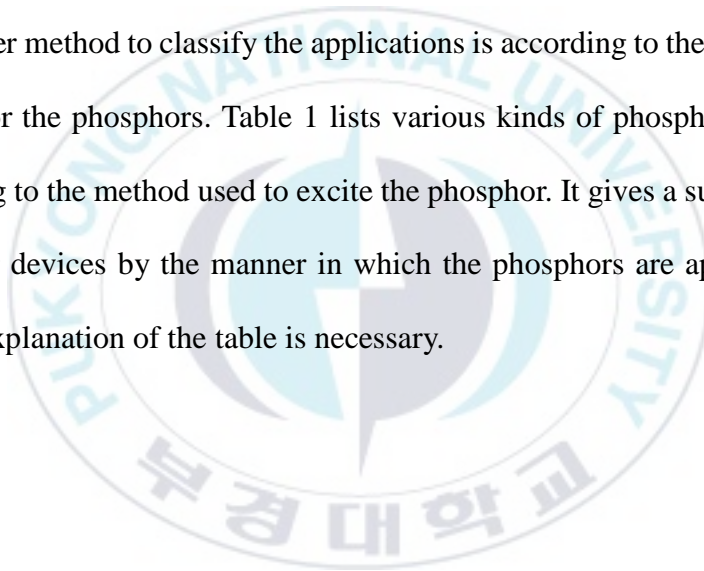
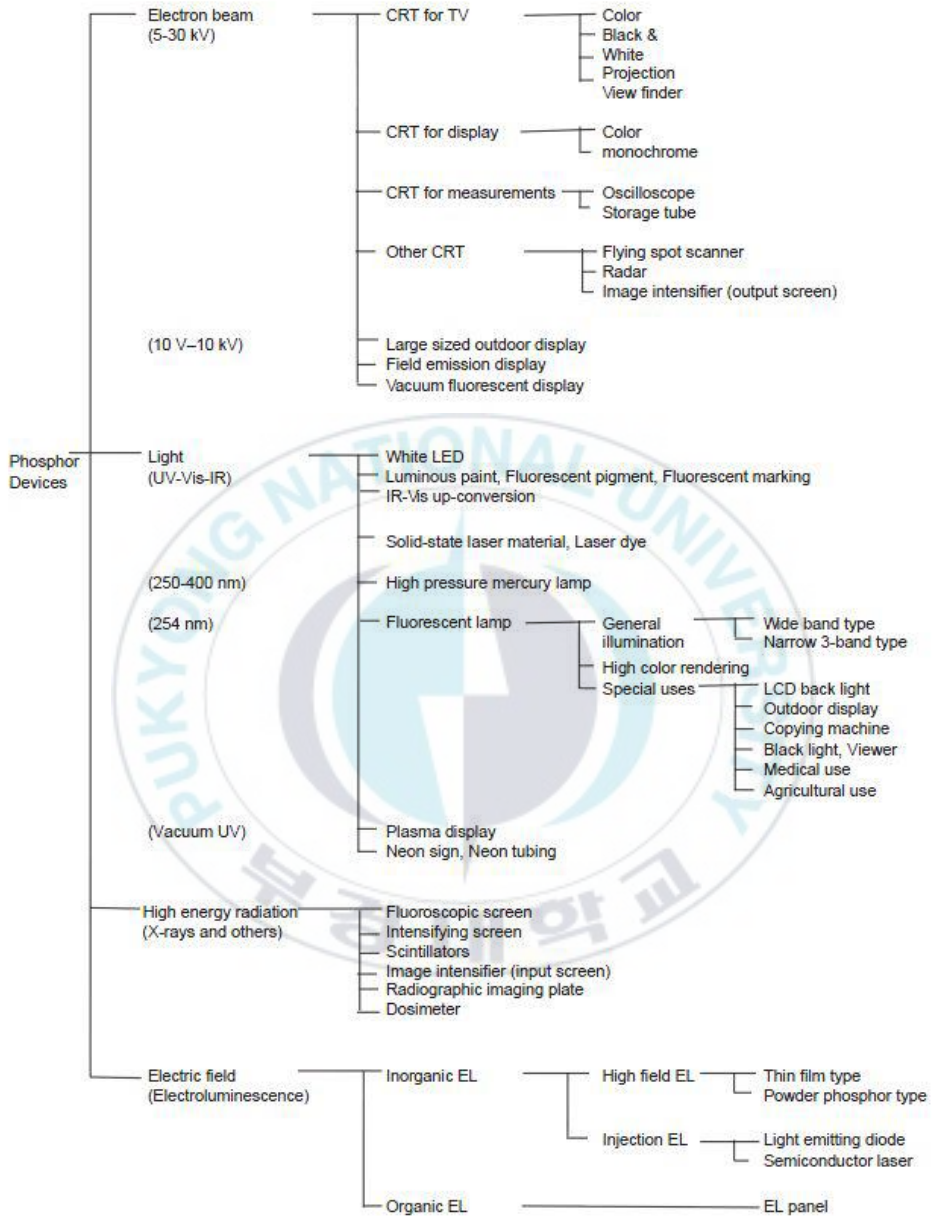


Table 2. 1 Phosphor device

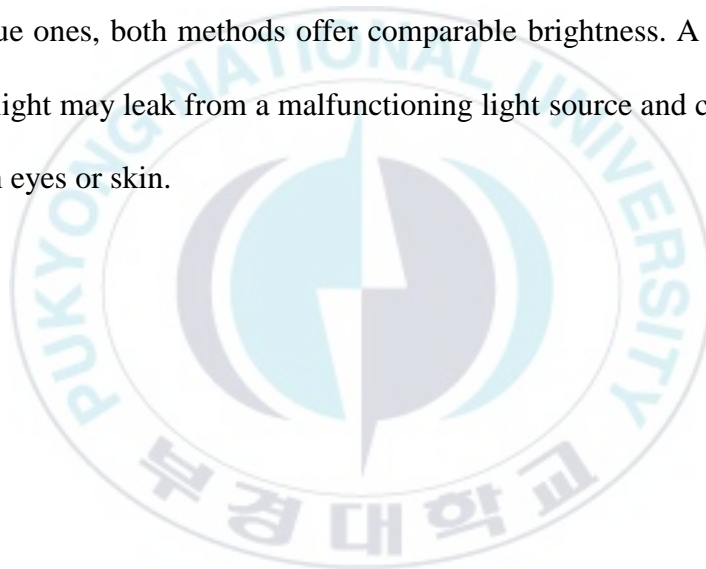


2. 1. 4 Phosphors based light emitting diode

This method involves the single color emitting LED (mostly blue LEDs made of InGaN) chip coating with phosphors of different colors to form white light; the resultant LEDs are called phosphor-based or phosphor-converted white LEDs (pcLEDs) [37]. A fraction of the blue light undergoes the Stokes shift being transformed from shorter wavelengths to longer. Depending on the color of the original LED, phosphors of different colors can be employed. If several phosphor layers of distinct colors are applied, the emitted spectrum is broadened, effectively raising the color rendering index (CRI) value of a given LED [22]. Phosphor-based LED efficiency losses are due to the heat loss from the Stokes shift and also other phosphor-related degradation issues. Their luminous efficacies compared to normal LEDs depend on the spectral distribution of the resultant light output and the original wavelength of the LED itself. For example, the luminous efficacy of a typical YAG yellow phosphor based white LED ranges from 3 to 5 times the luminous efficacy of the original blue LED because of the human eye's greater sensitivity to yellow than to blue (as modeled in the luminosity function). Due to the simplicity of manufacturing the phosphor method is still the most popular method for making high-intensity white LEDs. The design and production of a light source or light fixture using a monochrome emitter with phosphor conversion is simpler and cheaper than

a complex RGB system, and the majority of high-intensity white LEDs presently on the market are manufactured using phosphor light conversion. Among the challenges being faced to improve the efficiency of LED-based white light sources is the development of more efficient phosphors. As of 2010, the most efficient yellow phosphor is still the YAG phosphor, with less than 10% Stoke shift loss. Losses attributable to internal optical losses due to re-absorption in the LED chip and in the LED packaging itself account typically for another 10% to 30% of efficiency loss. Currently, in the area of phosphor LED development, much effort is being spent on optimizing these devices to higher light output and higher operation temperatures. For instance, the efficiency can be raised by adapting better package design or by using a more suitable type of phosphor. Conformal coating process is frequently used to address the issue of varying phosphor thickness. Some phosphor-based white LEDs encapsulate InGaN blue LEDs inside phosphor-coated epoxy. Alternatively, the LED might be paired with a remote phosphor, a preformed polycarbonate piece coated with the phosphor material. Remote phosphors provide more diffuse light, which is desirable for many applications. Remote phosphor designs are also more tolerant of variations in the LED emissions spectrum. A common yellow phosphor material is cerium-doped yttrium aluminium garnet (Ce³⁺:YAG). White LEDs can also be made by coating near-ultraviolet

(NUV) LEDs with a mixture of high-efficiency europium-based phosphors that emit red and blue, plus copper and aluminium-doped zinc sulfide (ZnS:Cu, Al) that emits green. This is a method analogous to the way fluorescent lamps work. This method is less efficient than blue LEDs with YAG:Ce phosphor, as the Stokes shift is larger, so more energy is converted to heat, but yields light with better spectral characteristics, which render color better. Due to the higher radiative output of the ultraviolet LEDs than of the blue ones, both methods offer comparable brightness. A concern is that UV light may leak from a malfunctioning light source and cause harm to human eyes or skin.



2. 2 Structure of GdSr₂AlO₅

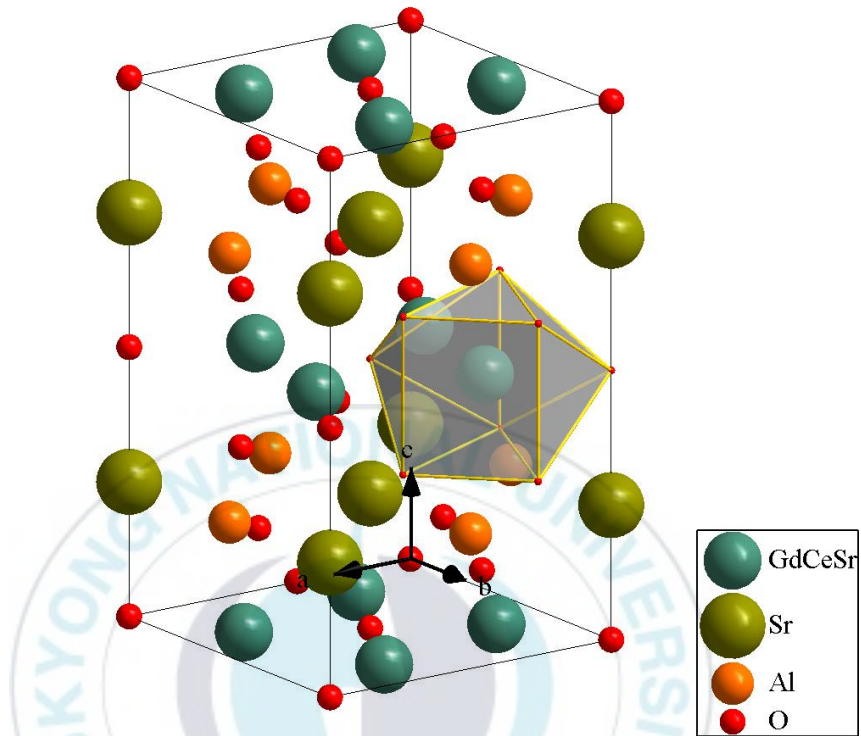


Figure 2. 2 Crystal structure of GdSr₂AlO₅:Ce³⁺.

Figure 3 displays the tetragonal crystal structure of GdSr₂AlO₅:Ce³⁺. The crystal structure of the GdSr₂AlO₅:Ce³⁺ belongs to the Cs₃CoCl₅-compound (tetragonal, space group I4/mcm), and is also similar structure to the (Ca, Sr, Ba)₃SiO₅ - type compounds (tetragonal, space group P4/ncc) [38]. In the unit cell (Z=4) of GdSr₂AlO₅:Ce³⁺, Ce and Gd atoms occupy only the 8h positions without other site substitution. The Ce and Gd atoms are settled in half 8h site, and half Sr atoms (Sr1) are occupied in other half 8h site. The cell also contains the 4a site fully occupied by Sr atoms (Sr2), and the

4b site filled by Al atoms. Oxygen atoms are distributed in the 4c site and the 16l site, denoted as O1 and O2, respectively. The CeO_8 polyhedron consists of two O1 atoms on the 4c site and six O2 atoms on the 16l site, where the latter are shared by four AlO_4 tetrahedra on the adjacent layers [25].



2. 3 The luminescence properties of Ce³⁺ in phosphor

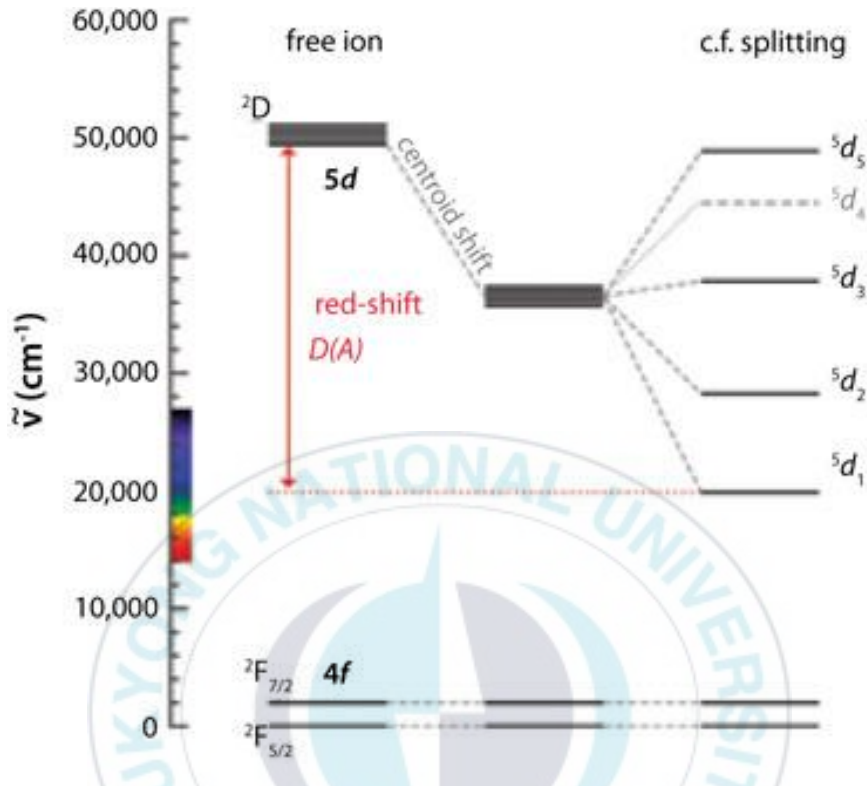
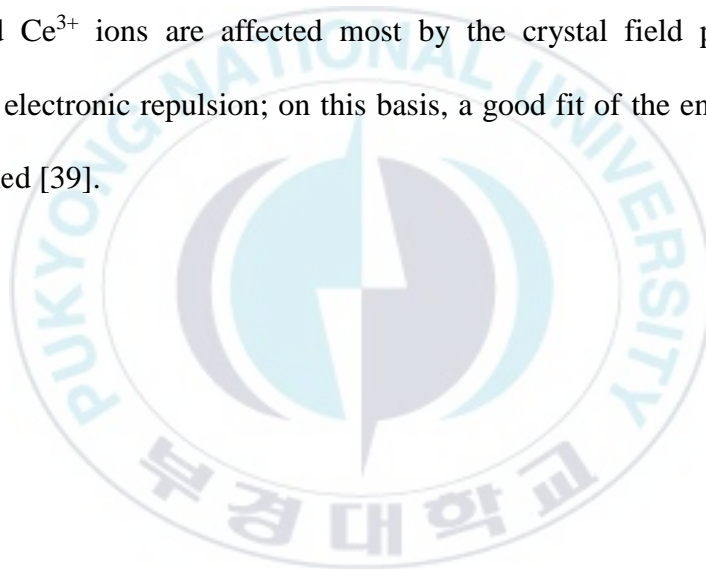


Figure 2. 3 Energy band of free Ce³⁺ ion and crystal field splitting that is occurred by host lattice.

The electronic configuration of Eu²⁺ ion is 4f⁷ and is identical to that of Gd³⁺ ion. The lowest excited state of 4f levels is located at about 28×10^3 cm⁻¹ and is higher than the 4f⁶5d¹ level in most crystals, so that Ce³⁺ ion usually gives broad-band emission due to f–d transitions. The wavelength range of the emission bands depend very much on hosts, changing from the near-UV to the red. Once introduced into a host lattice, the energy levels of the d-orbitals are reduced due to their interactions with the surrounding ligands (centroid shift due to the nephelauxetic effect). The crystal field

splitting, due to the varying interactions of the ligands with the different (xy , xz , yz , x^2-y^2 , z^2) d-orbitals, lifts the degeneracy and, in most structures, leads to as many as five states distinct in energy. The difference in energy between the d-states in the free ion and the lowest lying d-state in the crystalline host is called $D(A)$, or the spectroscopic red-shift. With increasing crystal field strength, the emission bands shift to longer wavelength. The luminescence peak energy of the $5d - 4f$ transitions of Eu^{2+} and Ce^{3+} ions are affected most by the crystal field parameters denoting electronic repulsion; on this basis, a good fit of the energies can be obtained [39].



2. 4 The effect of the Li⁺ co-doping in phosphor

Co-doping of Li⁺ in Eu²⁺/Ce³⁺ doped phosphors not only enhance the luminescence intensity but brings out changes even in the luminescence spectral ranges, so both these activators ions have been effectively studied in co-doping of Li⁺.

According to Grandhe et al. [40], the luminescence intensity of Na_{1-y}Li_yCa_{0.99}PO₄:0.01Eu²⁺ phosphors was improved by co-doping Li⁺. It is suggested that the difference in the ionic radius with Na⁺ and Li⁺ probably occur increase to diversity in the host lattice around the Eu²⁺.

Liu et al. [27] have synthesized the Li₂CaSiO₄:Eu²⁺ phosphor by a solid state reaction method and found that the Li⁺ makes optimum the excitation and emission characteristics of Eu²⁺ in host lattice also. Also, the high concentration of Li⁺ ions in the host lattice occur the distortion of the Eu²⁺-O²⁻ polyhedra (Li⁺ ions will disturb the expansion of the emission centers), which results in a smaller Stokes shift.

By Shen et al. the role of Li⁺ has been proposed in the Sr₃SiO₅:Ce³⁺ phosphor and found that the Li⁺ co-doping compensates the charge difference between the Ce³⁺ and Sr²⁺ ions and thus helps to incorporate the Ce³⁺ into Sr²⁺ sites.

Hao et al. [33] studied the luminescence properties of the CaO:Ce³⁺, Li⁺ phosphor. Compared with the Li⁺ un-doped CaO:Ce³⁺ phosphor, the Li⁺ co-

doped phosphor shows 1.88 times enhancement of luminescence intensity. Upon Li^+ ion co-doping the XRD peak intensity of CeO_2 decreases, indicating that more Ce^{4+} is converted to Ce^{3+} for effective doping into the CaO host lattice. This results in increased absorption of the excitation photons in $\text{CaO}:\text{Ce}^{3+}, \text{Li}^+$ occurring PL enhancement.

Jia et al. [32] have prepared the $\text{Lu}_2\text{SiO}_5:\text{Ce}^{3+}, \text{Li}^+$ phosphor. The PL intensity of $\text{Lu}_2\text{SiO}_5:\text{Ce}^{3+}, \text{Li}^+$ phosphor sample was 2.2 times higher than the $\text{Lu}_2\text{SiO}_5:\text{Ce}^{3+}$ phosphor. The $\text{Lu}_2\text{SiO}_5:\text{Ce}^{3+}$ has a two emission center, denoted to Ce1 and Ce2. The enhanced luminescence intensity of $\text{Lu}_2\text{SiO}_5:\text{Ce}^{3+}$ phosphors by Li^+ ion co-doping is mainly regarded as the result of the production of the local distortion in host lattice, which alters the crystal field around activator and results in the energy transfer from Ce2 to Ce1 centers.

Also, it was investigated that co-doping Li^+ affect to persistent/afterglow emission. As a result of the research performed by Kojima et al. [28], the afterglow intensity and afterglow time of $\text{CaS}:\text{Ce}^{3+}, \text{Pr}^{3+}$ both increase, by three and four fold, respectively. They found that co-doping the Li^+ ion makes new cation vacancy is formed for the charge compensation in the Ca^{2+} site, which increases the lattice strain. This cation vacancy acting as an electron trap can capture the excited electrons.

3. Experimental

3.1 Preparation of samples



Figure 3. 1 Schematic diagram of processing steps involved in synthesis of GdSr₂AlO₅:Ce³⁺ powder phosphors.

3. 1. 1 Preparation of $\text{Gd}_{1-x}\text{Sr}_2\text{AlO}_5:x\text{Ce}^{3+}$ (GSA: Ce^{3+}) using a high-energy ball milling

$\text{Gd}_{1-x}\text{Sr}_2\text{AlO}_5:x\text{Ce}^{3+}$ of different Ce^{3+} ion concentration ($x = 0.01, 0.02, 0.03, 0.05, 0.07$ and 0.10) were prepared via the high-energy ball milling method by taking the stoichiometric amounts of raw materials. Gd_2O_3 (Aldrich, 99.99%), SrCO_3 (Aldrich, 99.9%), CeO_2 (Aldrich, 99.9%) and Al_2O_3 (Kanto, 99%) were used as the starting materials. The high-energy ball milling process was implemented by using ethanol and hard zircon oxide balls (10 mm diameter, 25 ea) with 350 rpm rotation speed for 50 minutes and pause time for 10 min. This process was repeated 9 times sequentially. Ethanol and precursor mixture were dried by using an oven at $70\text{ }^\circ\text{C}$ during 24 hours. The dried precursor powder was grounded in an agate mortar. The precursor powder was annealed at $1600\text{ }^\circ\text{C}$ for 4 hours with the carbothermal reduction for increasing rate of $3\text{ }^\circ\text{C}/\text{min}$.

3. 1. 2 Preparation of $(\text{Gd}_{0.98}\text{Ce}_{0.02})\text{Sr}_2\text{AlO}_5:\text{xLi}^+$ (GSA: Ce^{3+} , Li^+) using a high-energy ball milling

A series of $(\text{Gd}_{0.98}\text{Ce}_{0.02})\text{Sr}_2\text{AlO}_5:\text{xLi}^+$ ($x = 0, 0.01, 0.02, 0.04, 0.06, 0.08, 0.10$; GSA: Ce^{3+} , Li^+) phosphors were also prepared by the high-energy ball milling method. Gd_2O_3 (Aldrich, 99.9%), SrCO_3 (Aldrich, 99.9%), CeO_2 (Aldrich, 99.9%), Al_2O_3 (Kanto, 99%) and Li_2CO_3 (Junsei, 99%) were used as the starting materials. After the weighing of starting materials, Ethanol and hard zirconia ball (10 mm diameter, 25ea) was added to mixture. The high-energy ball milling method was performed with 350 rpm rotation speed for 50 minutes and pause time for 10 min. this procedure was repeated 9 times, continuously. The ethanol and precursor mixture was dried in an oven at 70 °C for 1 day. The dried mixture was grounded in an alumina mortar. The precursor powder was preheated at 600 °C for 4h in order to avoid lithium volatilization. After the pre-heat process, the obtained products were annealed at 1600 °C for 4h. Both heating sequence was implemented with the carbothermal reduction with an increasing rate of 3°C/min.

3. 1. 3 Preparation of $(\text{Gd}_{0.95}\text{Ce}_{0.05})\text{Sr}_2\text{AlO}_5:\text{xLi}^+$ (GSA: Ce^{3+} , Li^+) using a sol-gel method

The $\text{Gd}_{0.95}\text{Ce}_{0.05}\text{Sr}_2\text{AlO}_5:\text{xLi}^+$ ($x = 0, 0.025, 0.050, 0.100, 0.150, 0.200, 0.250$) phosphors were prepared from $\text{Gd}(\text{NO}_3)_3 \cdot 6\text{H}_2\text{O}$ (Aldrich, 99.95%), $\text{Ce}(\text{NO}_3)_3 \cdot 6\text{H}_2\text{O}$ (Aldrich, 99.99%), $\text{Sr}(\text{NO}_3)_2$ (Aldrich, 98%), $\text{Al}(\text{NO}_3)_3 \cdot 9\text{H}_2\text{O}$ (Aldrich, 98%), LiNO_3 (Aldrich, 98%) as a starting materials and citric acid [$\text{HO}(\text{COOH})(\text{CH}_2\text{COOH})_2$] as a chelating agent. The starting materials were dissolved in deionized water and stirred with a magnetic stirrer for 4 h to make homogeneous mixture. The citric acid was melted into mixture and heated to 80 °C with 2°C/min of temperature increasing rate and held the temperature for 4 h with a magnetic stirring and closed cap. The mixture was evaporated and yellow translucent gel was produced after opening the cap. After that, the gel was dried at 120 °C for 24 h. The dry gel was pre-fired in a muffle furnace at 700 °C in air for 4 h to obtain a yellowish precursor. Annealing treatment of the precursor were performed at 1300 °C in tube furnace with reduction atmosphere (5% H_2 /95% Ar) for 4 h.

3. 2 High-energy ball milling process

In general, the most common synthesis method of phosphors is the solid-state reaction, which is cheap and simple to prepare. Nevertheless, the solid-state reaction method requires high synthesis temperature, and long heating process time and grinding after annealing process. High-energy ball milling method is an attractive method for preparing novel materials, which decreases the crystallite and particle sizes and leads the continuous formation of structural defects through the cycling pulverization and deformation of large crystallites [42, 43].

The figure below shows the motions of the balls and the powder. Since the rotation directions of the bowl and turn disc are opposite, the centrifugal forces are alternately synchronized. Thus friction resulted from the hardened milling balls and the powder mixture being ground alternately rolling on the inner wall of the bowl and striking the opposite wall. The impact energy of the milling balls in the normal direction attains a value of up to 40 times higher than that due to gravitational acceleration. Hence, the planetary ball mill can be used for high-speed milling.

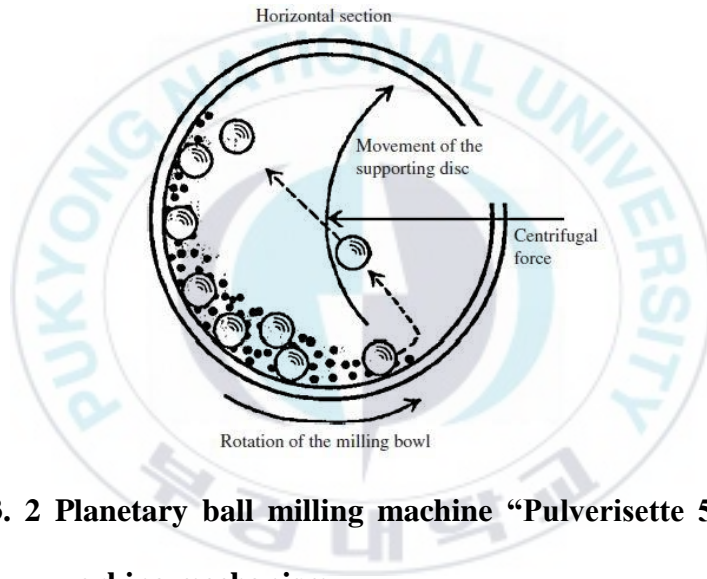


Figure 3. 2 Planetary ball milling machine “Pulverisette 5” and its working mechanism.

3. 3 Sol-gel method

The sol-gel process is a wet-chemical technique used for the fabrication of micro-crystalline, nano-crystalline and amorphous materials. In this process, the sol (or solution) is a stable suspension of colloidal solid particles or polymers in a liquid. And 'gel' is porous, three-dimensional, continuous solid network surrounding a continuous liquid phase. The 'sol' evolves gradually towards the formation of a gel-like network containing both a liquid phase and a solid phase. Typical precursors are metal alkoxides and metal chlorides, which undergo hydrolysis and poly-condensation reactions to form a colloid. Removal of the remaining liquid (solvent) phase requires a drying process, which is typically accompanied by a significant amount of shrinkage and densification. Afterwards, a thermal treatment, or firing process, is often necessary in order to favor further poly-condensation and enhance mechanical properties and structural stability via final sintering, densification and grain growth.

The sol-gel approach is a cheap and low-temperature technique that allows for the fine control of the product's chemical composition. Even small quantities of dopants, such as organic dyes and rare earth elements, can be introduced in the sol and end up uniformly dispersed in the final product. Sol-gel derived materials have diverse applications in optics, electronics, energy, space, (bio)sensors, medicine (e.g., controlled drug

release), reactive material and separation (e.g., chromatography) technology.

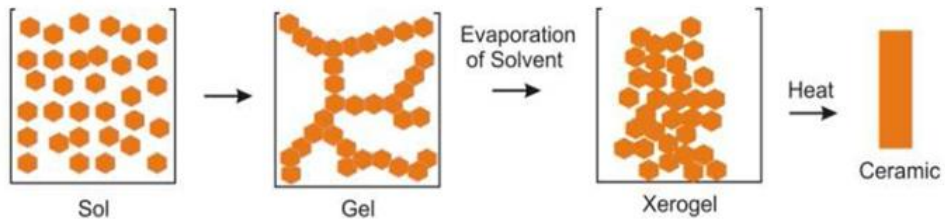


Figure 3. 3 Schematic representation of the sol-gel method.



3. 4 Characteristizations of the phosphors

The crystallization process of the complex precursors was examined by thermogravimetric – differential thermal analysis (TG-DTA, TGA7-DTA7, Perkin Elmer, Waltham, MA) using a 10 mg sample at a heating rate of 10 °C min⁻¹ in air. X-ray diffraction (XRD) pattern of the GSA:Ce³⁺ were measured by using the X-ray diffractometer (Philips, X'Pert-MPD system) with 3 kW Cu-K α ($\lambda=1.54056 \text{ \AA}$) X-ray tube in scattering angle of 15–70° for scan speed 2°/min. The surface morphology of GSA:Ce³⁺ was obtained by field emission scanning electron microscope (FE-SEM, JSM-6700, JEOL). The room temperature photoluminescence (PL) and photoluminescence excitation (PLE) spectra of the GSA:Ce³⁺ phosphors were measured on a PTI (Photon Technology International) fluorimeter by using a Xe-arc lamp with a power of 60 W. The prototype white LEDs were fabricated by using the GSA:Ce³⁺ phosphor, silicon resin and blue LED chips (465 nm dominant wavelength). Luminescence spectra and Commission Internationale de l'Eclairage (CIE) 1931 color coordinate from the white LEDs which generated under forward voltage (3.1 V) and forward current (20 mA) was obtained by an integrating sphere.



Figure 3. 4 Thermo Gravimetric - Differential Thermal Analyzer (Perkin Elmer TGA7-DTA7).



Figure 3. 5 X-ray diffractometer (Philips X'Pert/MPD).

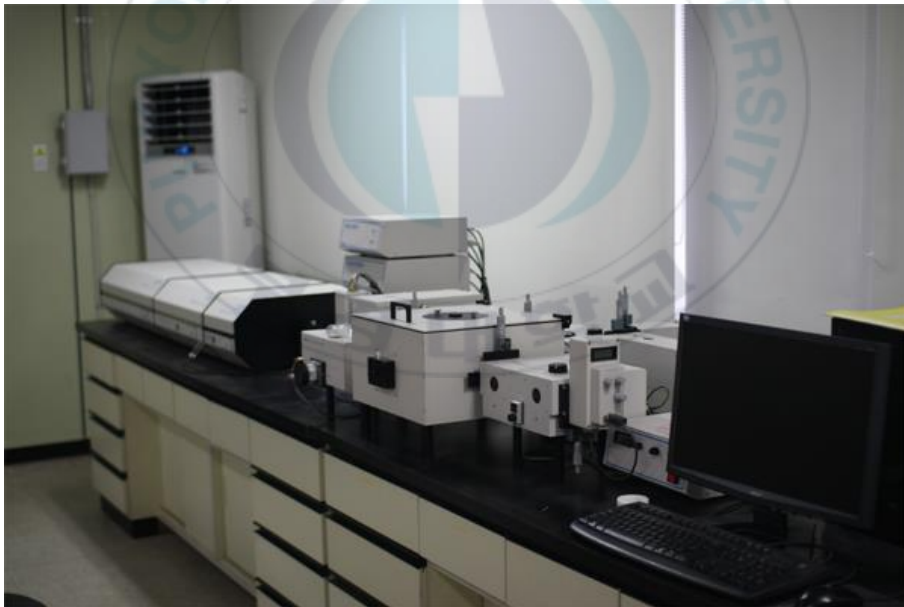


Figure 3. 6 Time resolved spectrometer system (PTI).



Figure 3. 7 Field emission scanning electron microscope (JEOL, JSM-6700F).

4. Result and discussions

4.1 $\text{Gd}_{1-x}\text{Sr}_2\text{AlO}_5:x\text{Ce}^{3+}$ prepared by high-energy ball milling

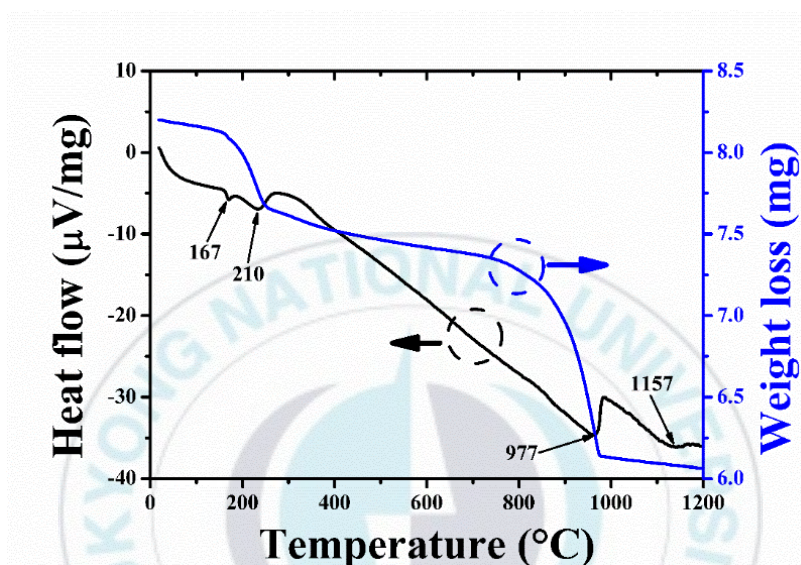


Figure 4. 1 TG/DTA curves of GSA:Ce³⁺ powder precursor in air.

Figure 4. 1 shows the TG-DTA curve for the GSA:Ce³⁺ powder precursor. The TG curve shows two distinct weight steps below 975 °C. No weight loss was observed between 975 °C and 1200 °C. The DTA curve reveals four endothermic peaks: at 167 °C, 210 °C, 977 °C, and 1157 °C. The first two peaks indicate the evaporation of water and organic species from the GSA:Ce³⁺ precursor, respectively. The third peak at 977 °C corresponds to the decomposition of strontium carbonate into strontium oxide and carbon dioxide. At 1157 °C, the weight loss was not appeared and the endothermic

peak was exhibited. It indicates that the chemical reaction of the GSA:Ce³⁺ precursor begins at 1157 °C.

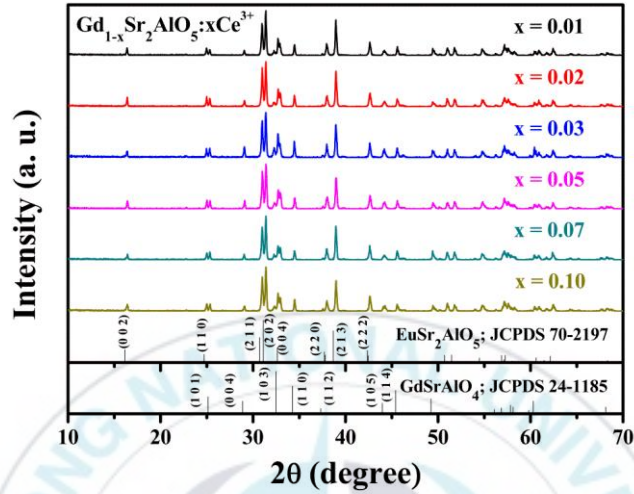


Figure 4. 2 X-ray diffraction patterns of GSA:Ce³⁺ for different Ce³⁺ concentration.

The XRD patterns of the GSA:Ce³⁺ phosphors with different Ce³⁺ concentrations are shown in Figure 4. 2. The diffraction peaks correspond to the GdSr₂AlO₅ main phase (close to the JCPDS 70-2197, a tetragonal phase with an *I4/mcm* space group) and GdSrAlO₄ impurity phase (JCPDS 24-1185, a tetragonal phase with a *I4/mmm* space group). In order to calculate the crystallite size of GSA:Ce³⁺ phosphors, three dominant XRD peaks {(2 1 1), (2 0 2), (2 1 3)} of the GdSr₂AlO₅ phase were used in the Scherrer's equation, $D = K\lambda/\beta\cos\theta$, where *D* is the average grain size (crystallite size), *K* is a shape factor (0.9), λ is the wavelength of the Cu-

$K\alpha$ radiation (1.5406 Å), β is the full width at half maximum (FWHM), and θ is the diffraction angle of a measured peak. The computed average grain size was found to be about 72 nm and uniform for various Ce^{3+} ion concentrations. Compared with the (2 0 2) peak, the relative intensity in the (2 1 1) crystal plane direction reaches the maximum value when the Ce^{3+} content is equal to 2 mol%. Increasing the Ce^{3+} concentration above 2 mol% decreases the relative XRD intensity in the (2 1 1) direction. The dominant peaks positions were not affected by the Ce^{3+} concentration.

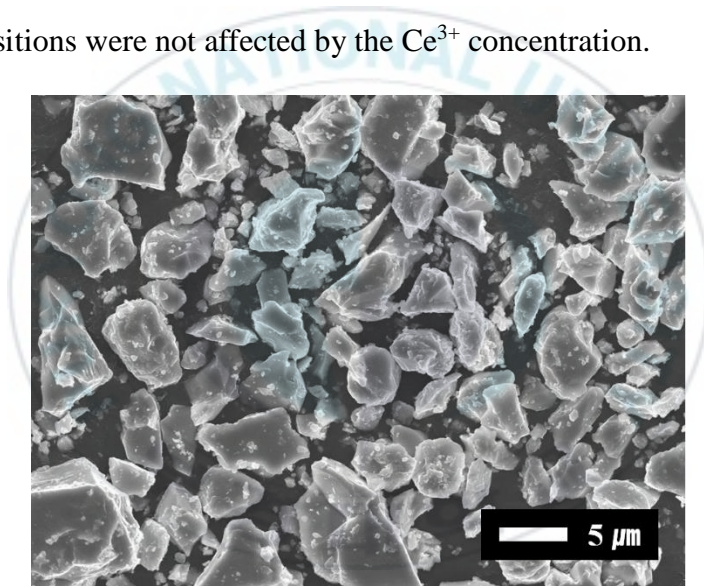


Figure 4. 3 FE-SEM image of $Gd_{0.98}Sr_2AlO_5:0.02Ce^{3+}$ phosphor.

Figure 4. 3 depicts the FE-SEM image of the $GSA:Ce^{3+}$ phosphor. Since the grinding occurred after the high-temperature annealing step, the $GSA:Ce^{3+}$ particles appear to have irregular shapes ranging from 5 to 7 micrometers in size. The particle morphology and sizes were also not affected by the Ce^{3+} concentration.

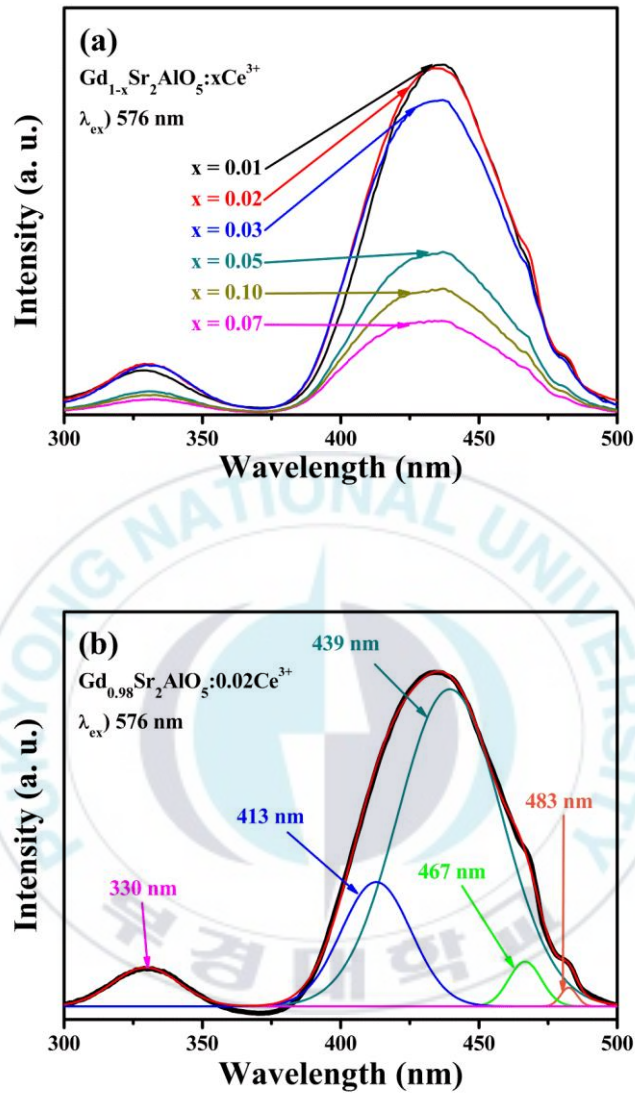


Figure 4. 4 (a) PLE spectra ($\lambda_{em} = 576$ nm) of GSA: Ce^{3+} phosphor for different Ce^{3+} ion concentration and (b) Gaussian function fitting graph of PLE spectra for $Gd_{0.98}Sr_2AlO_5:0.02Ce^{3+}$ phosphor.

Figure 4. 4 shows the effect of the Ce^{3+} concentration on the PLE spectra

(Figure 4. 4 (a)) and the Gaussian fitting curves (Figure 4. 4 (b)) for the 5d energy levels of Ce^{3+} ions in the GSA: Ce^{3+} phosphors. The excitation spectra possess a dominant excitation intensity between 375 and 500 nm, which matched with the emission spectra for InGaN blue LED chips. The dominant excitation intensity (at 438 nm) reaches a maximum at a Ce^{3+} concentration of 2 mol%. The excitation peaks result from the transition between the ground state ($^2F_{5/2}$) and the split 5d energy states and are well matched with the clear peak measurements between 300 nm and 500 nm. The PLE spectra consist of one dominant peak at 438 nm and four weaker peaks at 330 nm, 413 nm, 467 nm, and 483 nm. The five Gaussian peak positions and dominant excitation wavelength do not shift when the Ce^{3+} ion content increases. The centroid shift, defined as the difference in energy between the 5d state of free Ce^{3+} ions and the lowest occupying 5d state of the Ce^{3+} ions in the crystalline host lattice, was calculated to be 30300 cm^{-1} . The crystal splitting (defined as the difference between the highest and lowest cerium energy states) was estimated to be 15300 cm^{-1} .

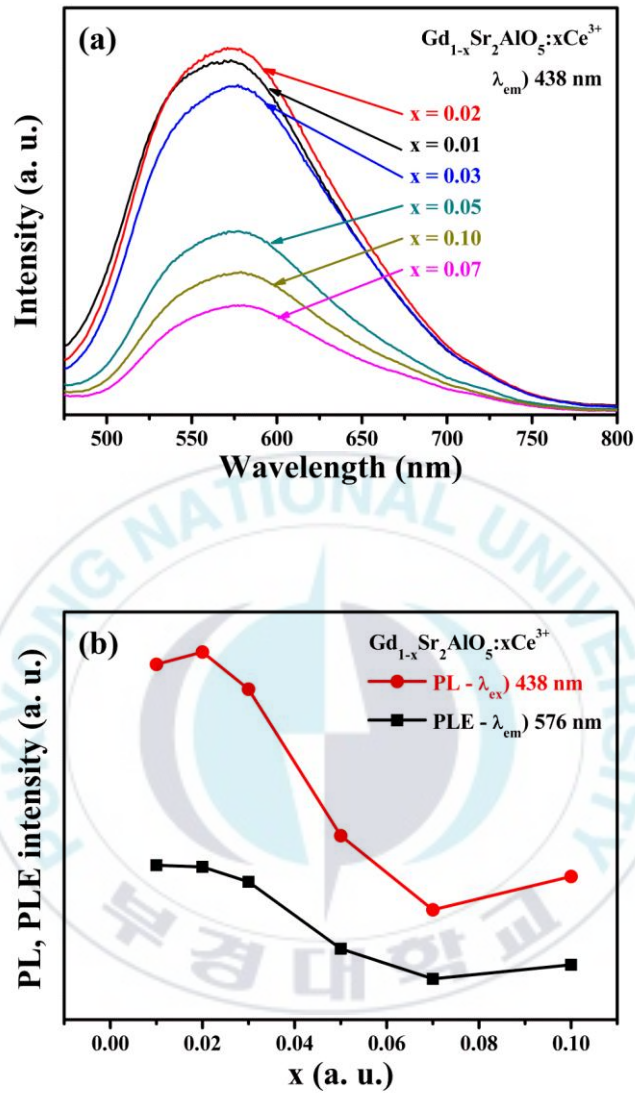


Figure 4. 5 (a) PL spectra ($\lambda_{ex} = 438$ nm) and (b) maximum PL and PLE intensity of GSA:Ce³⁺ phosphors as a function of Ce³⁺ ion concentration.

Figure 4. 5 shows the effect of Ce³⁺ concentration on (a) the PL spectra and (b) the PL/PLE intensities in the GSA:Ce³⁺ phosphors. The emission

spectra reach maximum intensity at 576 nm and are characterized by a broad emission band extending from 475 nm through 750 nm, which indicates that yellow phosphor can be pumped with an InGaN blue chip. The estimated Stoke shift of the $\text{Gd}_{0.98}\text{Sr}_2\text{AlO}_5:0.02\text{Ce}^{3+}$ phosphor is 4830 cm^{-1} due to the crystal field generated by the GSA host lattice. The emission intensity increases with the Ce^{3+} ion concentration and reaches its maximum value at 2 mol%. Increasing the Ce^{3+} ion concentration beyond 2 mol% results in a decrease of the emission intensity due to concentration quenching. The doping concentration determines the distance between Ce^{3+} ions in the phosphor, which, in turn, affects the interaction strength leading to concentration quenching. The critical distance for energy transfer (R_C) between activator ions of the same kind in a GSA host lattice can be calculated using the Blasse's equation [20]: $R_C \approx 2\left(\frac{3V}{4\pi x_C N}\right)^{1/3}$, where R_C corresponds to the distance between the nearest Ce^{3+} ions at the critical concentration, V is the volume of the unit cell, N is the number of cations in the unit cell, and x_C is the critical concentration of activator ions. Using the parameters for the crystal structure of $\text{GdSr}_2\text{AlO}_5$ ($V = 492.68\text{ \AA}^3$, $N = 4$ and $x_C = 0.02$), the calculated R_C is found to be about 23 \AA .

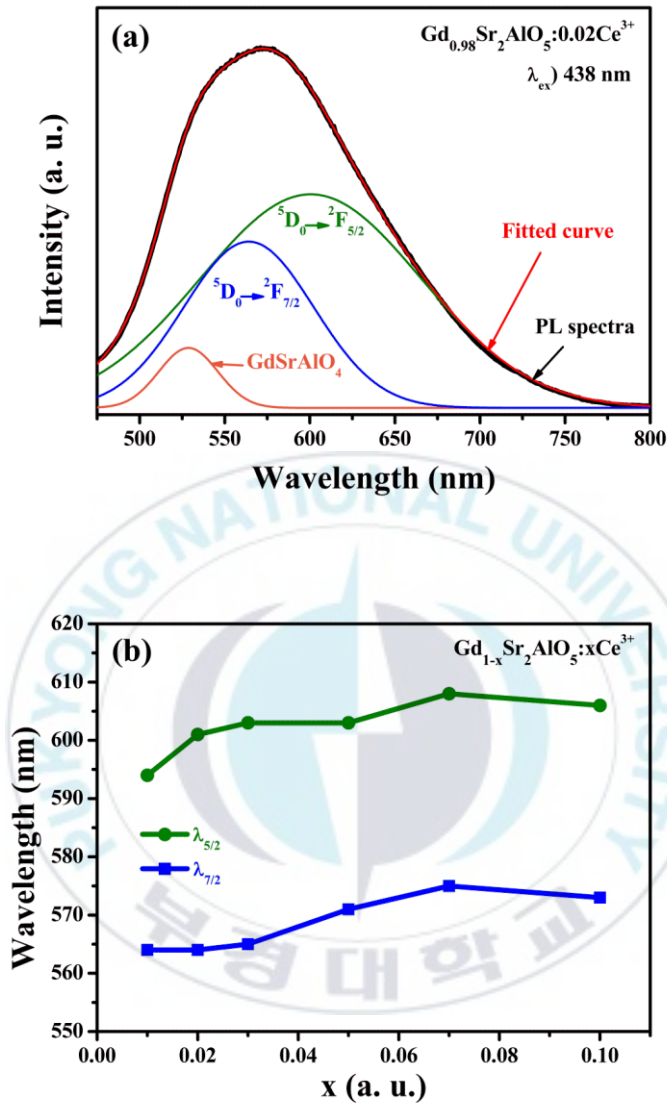


Figure 4. 6 (a) Gaussian function fitting graph of PL spectra for $\text{Gd}_{0.98}\text{Sr}_2\text{AlO}_5:0.02\text{Ce}^{3+}$ phosphor and (b) Gaussian function peak as a function of Ce^{3+} ion concentration.

Gaussian deconvolution of the PL spectra is shown in Figure 4. 6. The spectra were fitted by the sum of three Gaussian functions since the

GSA:Ce³⁺ phosphor has a GdSrAlO₄ impurity phase. The first Gaussian peak (around 525 nm) is due to the GdSrAlO₄:Ce³⁺ phase impurity, and the last two peaks (at 564 nm and 601 nm) originate from the GSA:Ce³⁺ phosphor (GdSr₂AlO₅ main phase) due to the spin orbit coupling of Ce³⁺ ions. The positions of the last two Gaussian peaks indicate that Ce³⁺ ions substitute the Gd³⁺/Sr²⁺ 8h sites in GdSr₂AlO₅:Ce³⁺ phosphors. The Gaussian peaks of the GSA:Ce³⁺ phosphor shift to the red region when the Ce³⁺ concentration increases. The ionic radius of Gd³⁺ (1.043 Å) is smaller than that of Ce³⁺ (1.143 Å), resulting in a shorter bonding distance between Gd³⁺ ions compared to the Ce³⁺ ions. Using the point charge model the d-orbital splitting can be calculated with a simple equation [21]: $Dq = ze^2r^4/6a^5$, where Dq is a measure of crystal field splitting, z is the charge of the anion, e is the charge of an electron, r is the radius of the d-wavefunction, and a is the bond length. A high Ce³⁺ ion concentration leads to a greater magnitude of crystal field splitting due to the shorter distances between the neighbor ions. As a result, the band gap becomes narrower, and the Gaussian peaks shift towards the red region. Although the Gaussian peaks shift to the longer wavelength region, no shift occurs for the dominant wavelength of the PL spectra.

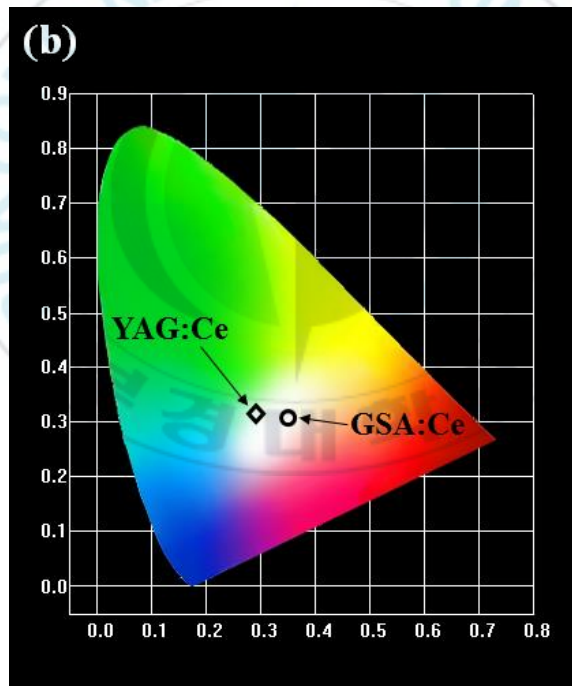
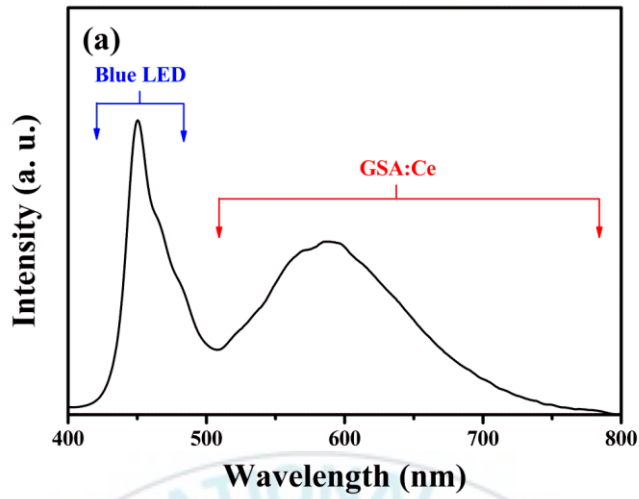


Figure 4. 7 (a) Emission spectra of fabricated white LEDs (blue LED chip + $\text{Gd}_{0.98}\text{Sr}_2\text{AlO}_5:0.02\text{Ce}^{3+}$ phosphor), (b) CIE 1931 color coordinate of fabricated white LEDs and commercial white LEDs (blue LED chip + YAG:Ce phosphors).

Table 4. 1 CIE 1931 color coordinate and color temperature of YAG:Ce³⁺ phosphors and GSA:Ce³⁺ (Gd_{0.98}Sr₂AlO₅:0.02Ce³⁺) phosphors encapsulated white LEDs, respectively.

Encapsulated phosphor	CIE 1931 coordinates	Color temperature (K)
YAG:Ce ³⁺	(0.290, 0.317)	8086
GSA:Ce ³⁺	(0.347, 0.311)	4719

Figure 7 shows (a) the emission spectra and (b) the CIE 1931 chromaticity coordinates for white LEDs fabricated using blue LEDs (excitation at 460 nm) and the Gd_{0.98}Ce_{0.02}Sr₂AlO₅ phosphor. The CIE color coordinates and color temperature of the fabricated white LED are (0.347, 0.311) and 4719 K, respectively. Compared with commercial white LEDs [22], the fabricated white LEDs exhibit better color rendering index due to the enhancement of red emission. Therefore, GSA:Ce³⁺ is a promising yellow phosphor that can be potentially used for general lighting.

4. 2 $(\text{Gd}_{0.98}\text{Ce}_{0.02})\text{Sr}_2\text{AlO}_5:x\text{Li}^+$ prepared by high-energy ball milling

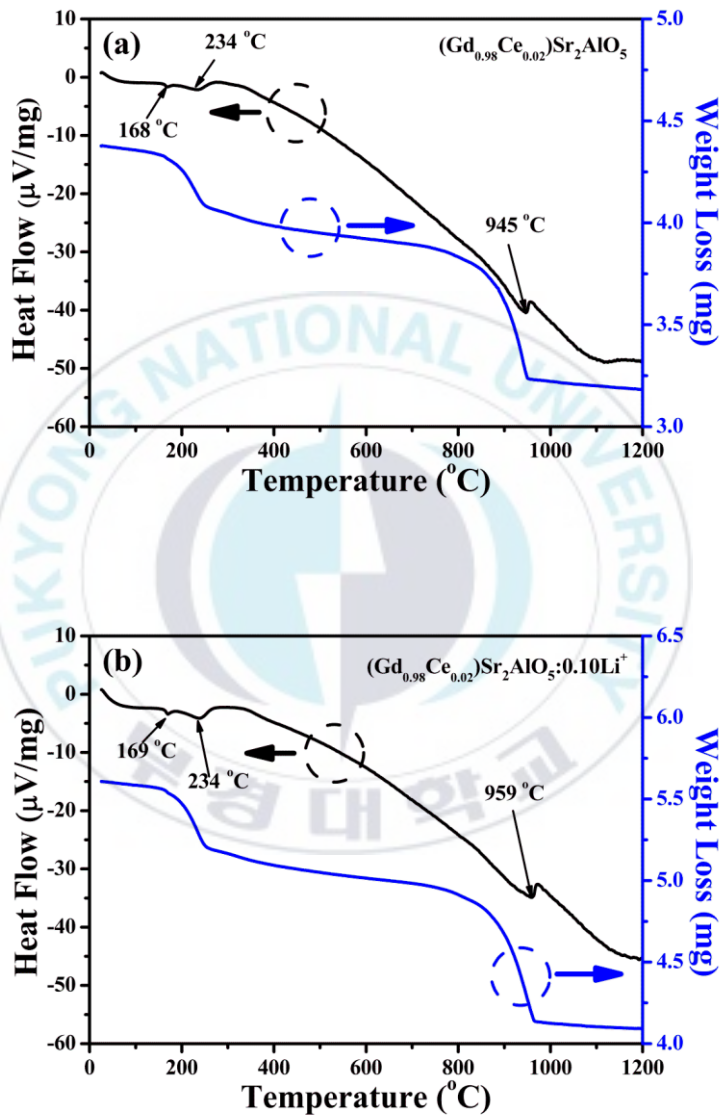


Figure 4. 8 TG/DTA curves of GSA: Ce^{3+} , Li^+ phosphors where (a) $x = 0$ and (b) $x = 0.10$.

Figure 4. 8 shows the TG/DTA curves of the powder precursor of GSA:Ce³⁺, Li⁺ phosphors where (a) x = 0 and (b) x = 0.10. The TG curve exhibits two weight loss steps upto 950 °C. The DTA curve exhibits three endothermic peaks at 168 °C, 234 °C and 945 °C. The first two peaks are corresponds to the evaporation of water and organic species on the surface of the precursor powder. The last peak at 945 °C indicate the decomposition of the strontium carbonate into strontium oxide and carbon dioxide. TG/DTA curves in Figure. 4. 8 (b) is analogous with the Figure 4. 8 (a) due to the low quantities of lithium carbonate in the precursor.

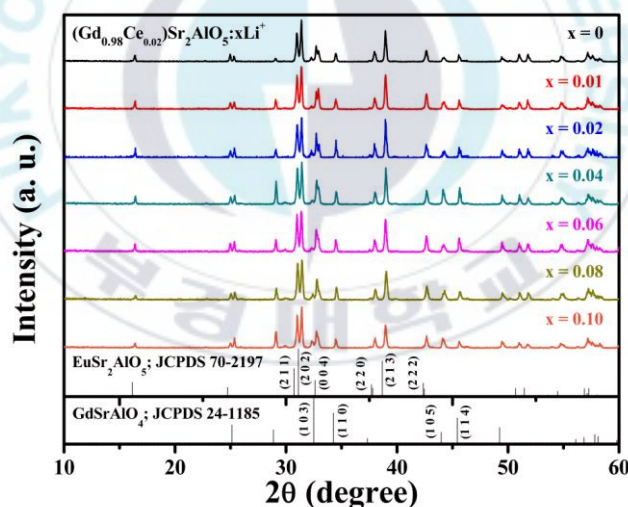


Figure 4. 9 X-ray diffraction patterns of GSA:Ce³⁺, Li⁺ for different Li⁺ concentration.

The XRD patterns of GSA:Ce³⁺, Li⁺ phosphors with different Li⁺ concentrations are shown in Figure. 4. 9. The diffraction patterns

correspond to the $\text{GdSr}_2\text{AlO}_5$ main phase (close to the JCPDS 70-2197; tetragonal phase with a $I4/mcm$ space group) phase and GdSrAlO_4 impurity phase (JCPDS 24-1185; tetragonal phase with a $I4/mmm$ space group). To calculate the crystallite size of $\text{GSA}:\text{Ce}^{3+}, \text{Li}^+$ phosphors, three dominant XRD peaks (2 1 1, 2 0 2, 2 1 3) of the $\text{GdSr}_2\text{AlO}_5$ phase were used in the Scherrer's equation, $D = K\lambda/\beta\cos\theta$, where D is the average crystallite size, K is a shape factor (0.9), λ is the wavelength of $\text{Cu-K}\alpha$ radiation (1.5406 Å), β is the full width at half maximum (FWHM) of XRD peak and θ is the diffraction angle of an measured peak. The calculated average crystallite size was 60 nm and constant for various Li^+ concentrations. Also, the positions of XRD peaks were not moved by Li^+ concentration. Nevertheless, compared with the (2 0 2) peak, relative intensity in the (2 1 1) and (2 1 3) crystal plane is changed with the Li^+ concentration. These results essentially regarded as the result of the crystal field distortion by co-doping Li^+ ion in $\text{GdSr}_2\text{AlO}_5$ host lattice [32].

Figure 4. 10 displays the FE-SEM images of $\text{GSA}:\text{Ce}^{3+}, \text{Li}^+$ phosphors where (a) $x = 0$ and (b) $x = 0.10$. The morphology of the both phosphors exhibit irregular shape and 10 μm size due to the grinding after sintering process. The effect of Li^+ co-doping in morphology of were not changed for Li^+ contents in $\text{GSA}:\text{Ce}^{3+}, \text{Li}^+$ phosphors. According to the former studies [31], the lithium carbonate can act as a flux which grows the particle

size of phosphors. The particle size and shape of the phosphors are one the factors which determine the luminescence intensity of phosphors. Nevertheless, Figure. 4. 8 (a) and (b) show that the contents of the lithium carbonate were not affect the particle size and shape.

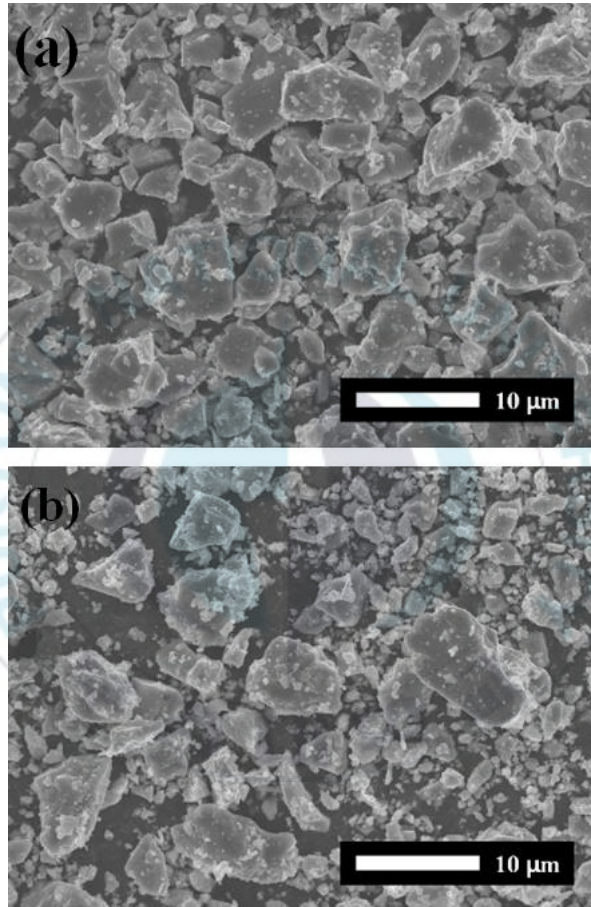


Figure 4. 10 FE-SEM images of GSA:Ce³⁺, Li⁺ phosphors where (a) x = 0 and (b) x = 0.10.

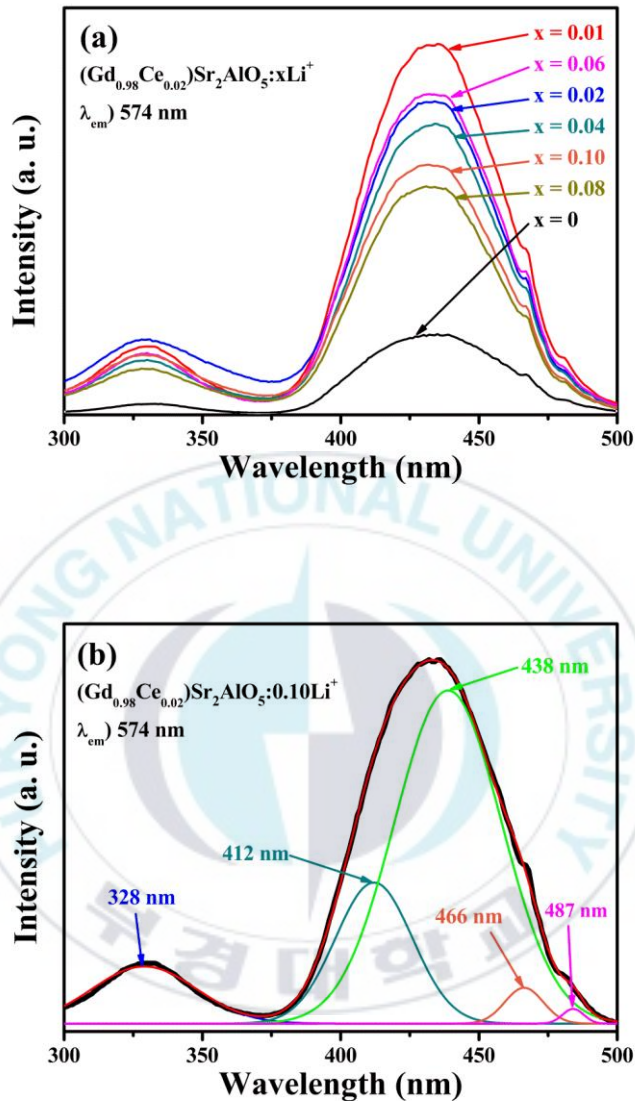


Figure 4. 11 (a) PLE spectra ($\lambda_{\text{em}} = 574 \text{ nm}$) of GSA: Ce^{3+} , Li^+ phosphor for different Li^+ ion concentration and (b) Gaussian function fitting graph of PLE spectra for $\text{Gd}_{0.98}\text{Ce}_{0.02}\text{Sr}_2\text{AlO}_5:0.10\text{Li}^+$ phosphor.

Figure 4. 11 shows the (a) PLE spectra of GSA: Ce^{3+} , Li^+ phosphors and

(b) gaussian fitting curves of the PLE spectra where $x = 0.10$. The most dominant excitation band between 375 and 500 nm matches with the emission spectra of InGaN LED chip due to the excitation spectra exhibit the highest intensity at 437 nm regardless of the Li^+ contents. The highest excitation intensity was obtained to 4.6 times higher than at $x = 0.01$. As x reaches to 0.01, 4.6 times enhancement of excitation intensity was obtained in comparison of the Li^+ un-doped GSA: Ce^{3+} phosphors. The excitation intensity was decreased as the x was further increase 0.01. The 5d energy levels of Ce^{3+} ion were analyzed by Gaussian functions to calculate the five different energy levels of Ce^{3+} ions. The calculated wavelength corresponding with the energy level of the Ce^{3+} ion are 328 nm, 412 nm, 438 nm, 466 nm and 487 nm. The excitation spectra were not shifted for different Li^+ concentration. Also, the calculated energy levels were constant regardless of the Li^+ contents. The calculated crystal splitting energy of GSA: Ce^{3+} , Li^+ phosphors was 10000 cm^{-1} .

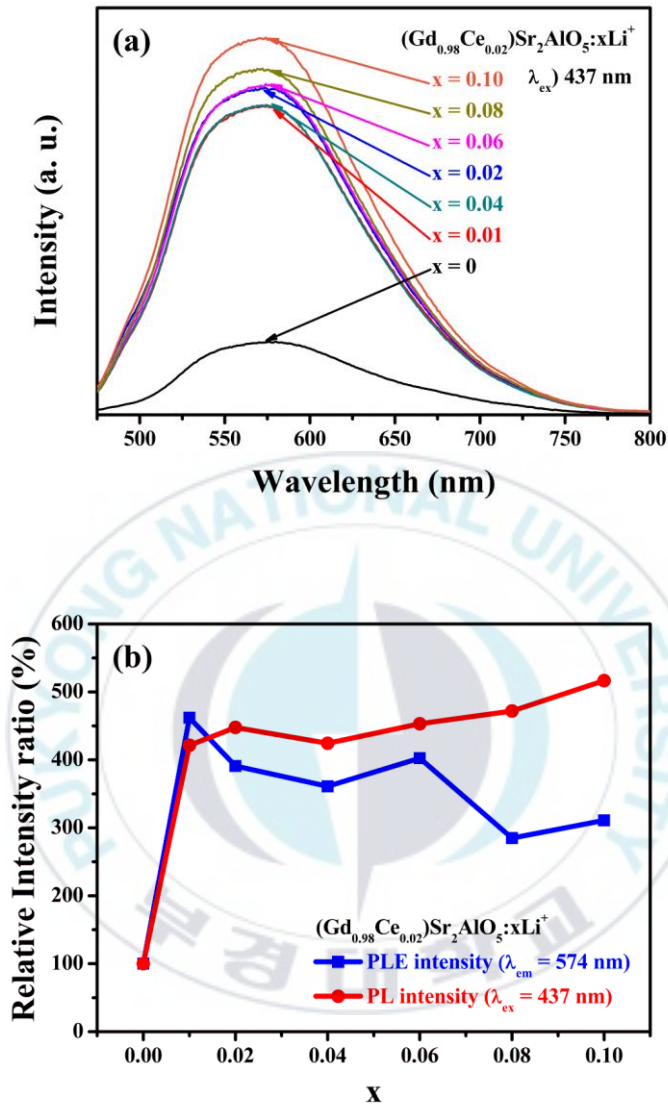


Figure 4. 12 (a) PL spectra ($\lambda_{\text{ex}} = 437 \text{ nm}$) and (b) maximum PL and PLE intensity of GSA: Ce^{3+} , Li^+ phosphors as a function of Li^+ ion concentration.

Figure 4. 12 displays the effect of the Li^+ concentration in (a) PL spectra and (b) comparison of PL intensity and PLE intensity of GSA: Ce^{3+} , Li^+

phosphors. The emission spectra was measured to be a broad band centered at 576 nm that can be used for yellow phosphors in white LEDs pumped by blue InGaN LED chips. Compared with $x = 0$, 5.17 times enhancement of PL intensity was obtained by increasing x up to 0.10. These enhancement can ascribed to substitution of Li^+ ion into the $\text{GSA}:\text{Ce}^{3+}$ host lattice. Co-doping Li^+ ions in Ce^{3+} doped phosphors can give local distortion in host lattice that can optimizing the environment around the Ce^{3+} ions [32].



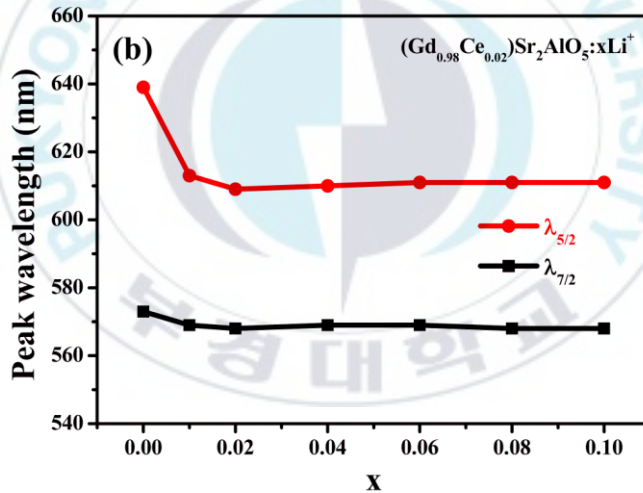
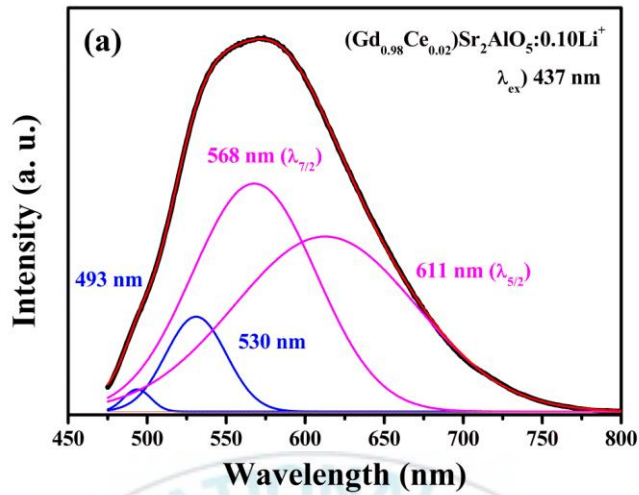


Figure 4. 13 (a) Gaussian function fitting graph of PL spectra for $Gd_{0.98}Ce_{0.02}Sr_2AlO_5:0.10Li^+$ phosphor and (b) Gaussian function peak as a function of Li^+ ion concentration.

Figure 4. 13 exhibits the (a) comparison of the calculated 5d-4f transition energy for Li^+ concentration and (b) Gaussian deconvolution of PL spectra

where $x = 0.10$. The emission band of Ce^{3+} ions strongly depends on the local environment of the activator ion. The 5d-4f transitions of Ce^{3+} ions generally occurs from the lowest 5d energy level to $^4\text{F}_{7/2}$ and $^4\text{F}_{5/2}$ energy level. The PL spectra was well matched by sum of four Gaussian function. The first two Gaussian peaks centered at 493 nm and 530 nm were the emission bands of Ce^{3+} doped GdSrAlO_4 phase. The emission band of Ce^{3+} doped $\text{GdSr}_2\text{AlO}_5$ phase were consist of two Gaussian peaks centered at 568 nm and 611 nm. The wavelength of 5d-4f transition energy in shifted from (573 nm, 639 nm) to (569 nm, 611 nm) by co-doping Li^+ ions. The wavelength related with 5d-4f transitions of Ce^{3+} ion were not shifted as the x is further increased above 0.01. The estimated spin-orbital coupling changed from 1852 cm^{-1} to 1288 cm^{-1} and the calculated Stoke shift altered from 3058 cm^{-1} to 2739 cm^{-1} by co-doping Li^+ ions in $\text{GSA}:\text{Ce}^{3+}$ phosphors. The change of the energy level of $\text{GSA}:\text{Ce}^{3+}$ by Li^+ ion doping were represented in Figure 4. 14.

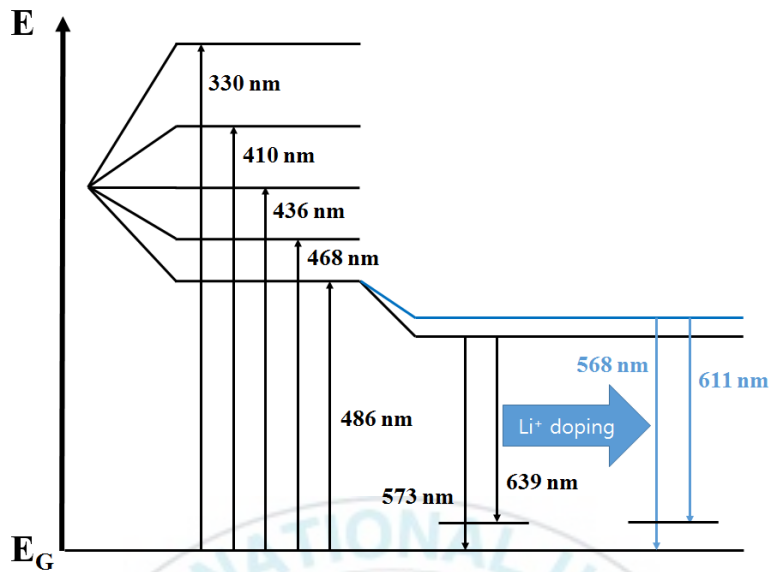


Figure 4. 14 Schematic diagram of energy level alteration by Li^+ co-doping in $\text{GSA}:\text{Ce}^{3+}$.

White LEDs were fabricated using $\text{GSA}:\text{Ce}^{3+}$ ($x = 0$) and $\text{GSA}:\text{Ce}^{3+}, \text{Li}^+$ ($x = 0.10$) phosphors combinations together with InGaN LEDs ($\lambda_{\text{max}} = 460$ nm), respectively. Figure 4. 15 shows the comparison of the (a) luminescence spectra and (b) CIE chromaticity. The calculated CIE color coordinates and color rendering index (CRI) were also displayed in Table 1. The yellow emission of the $\text{GSA}:\text{Ce}^{3+}, \text{Li}^+$ encapsulated white LEDs was enhanced in comparison of the $\text{GSA}:\text{Ce}^{3+}$ used white LEDs. In comparison of the white LEDs ($R_a = 78$, CCT = 10281K) encapsulated $\text{GSA}:\text{Ce}^{3+}$ phosphors, applying $\text{GSA}:\text{Ce}^{3+}, \text{Li}^+$ phosphor ($x = 0.10$) in white LEDs ($R_a = 83$, CCT = 4333K) exhibited better color rendering.

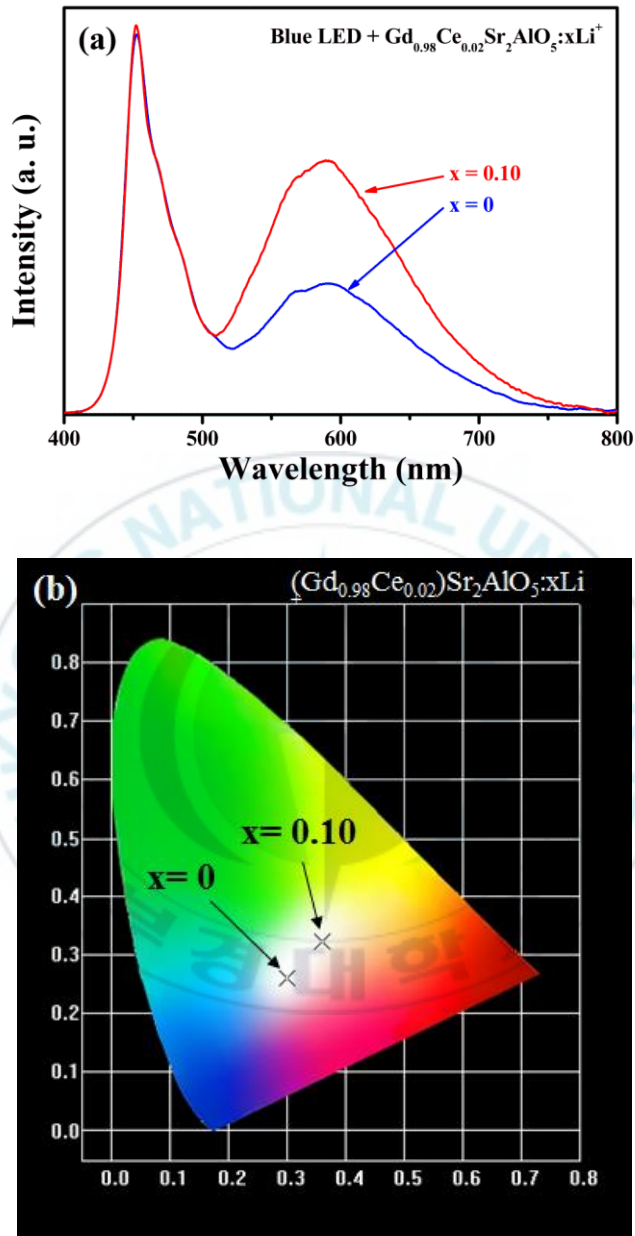


Figure 4. 15 Comparison of the (a) Emission spectra and (b) CIE 1931 color coordinate of fabricated white LEDs (blue LED chip + GSA: Ce^{3+} , blue LED chip + GSA: Ce^{3+} , Li^+ ; $x = 0.10$).

Table 4. 2 CIE 1931 color coordinate and color temperature of GSA:Ce³⁺ (Gd_{0.98}Ce_{0.02}Sr₂AlO₅) phosphors and GSA:Ce³⁺, Li⁺ (Gd_{0.98}Ce_{0.02}Sr₂AlO₅:0.10Li⁺) phosphors encapsulated white LEDs, respectively.

Encapsulated phosphor	CIE 1931 coordinates	Color temperature (K)
GSA:Ce ³⁺	(0.290, 0.317)	8086
GSA:Ce ³⁺ , Li ⁺	(0.347, 0.311)	4719



4. 3 ($\text{Gd}_{0.95}\text{Ce}_{0.05}\text{Sr}_2\text{AlO}_5:x\text{Li}^+$ prepared by sol-gel method

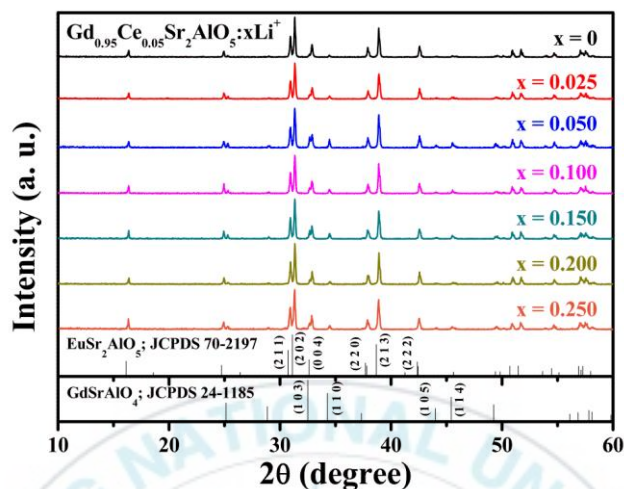


Figure 4. 16 X-ray diffraction patterns of GSA:Ce³⁺, Li⁺ phosphor for different Li⁺ concentration.

Figure 4. 16 shows the XRD patterns of GSA:Ce³⁺, Li⁺ phosphor with different Li⁺ concentration. The diffraction peaks matches to the GdSr₂AlO₅ main phase (close to the JCPDS 70-2197, a tetragonal phase with an *I4/mcm* space group) and GdSrAlO₄ impurity phase (JCPDS 24-1185, a tetragonal phase with a *I4/mmm* space group). To calculate the crystallite size of GSA:Ce³⁺, Li⁺ phosphor, three dominant XRD peaks (2 1 1, 2 0 2, 2 1 3) of the GdSr₂AlO₅ phase were used in the Scherrer's equation, $D = K\lambda/\beta\cos\theta$, where *D* is the average grain size (crystallite size), *K* is a shape factor (0.9), λ is the wavelength of the Cu-K α radiation (1.5406 Å), β is the full width at half maximum (FWHM), and θ is the diffraction angle of a measured

peak. The calculated average grain size was found to be 73 nm and constant for Li^+ concentration. Compared with Figure 4. 2 and 4. 9, the crystallinity of GdSrAlO_4 phase was decreased. The XRD peak position were not moved by the Li^+ concentration. The FE-SEM images of $\text{GSA}:\text{Ce}^{3+}, \text{Li}^+$ phosphor with different Li^+ concentration are shown in Figure 4. 17. The particles of $\text{GSA}:\text{Ce}^{3+}$ phosphors (Figure 4. 17 (a)) were spherical and hundreds nanometer size. With increasing the Li^+ concentration, spherical particles began to grow from hundreds nanometer to sub-micrometer and aggregate each other.



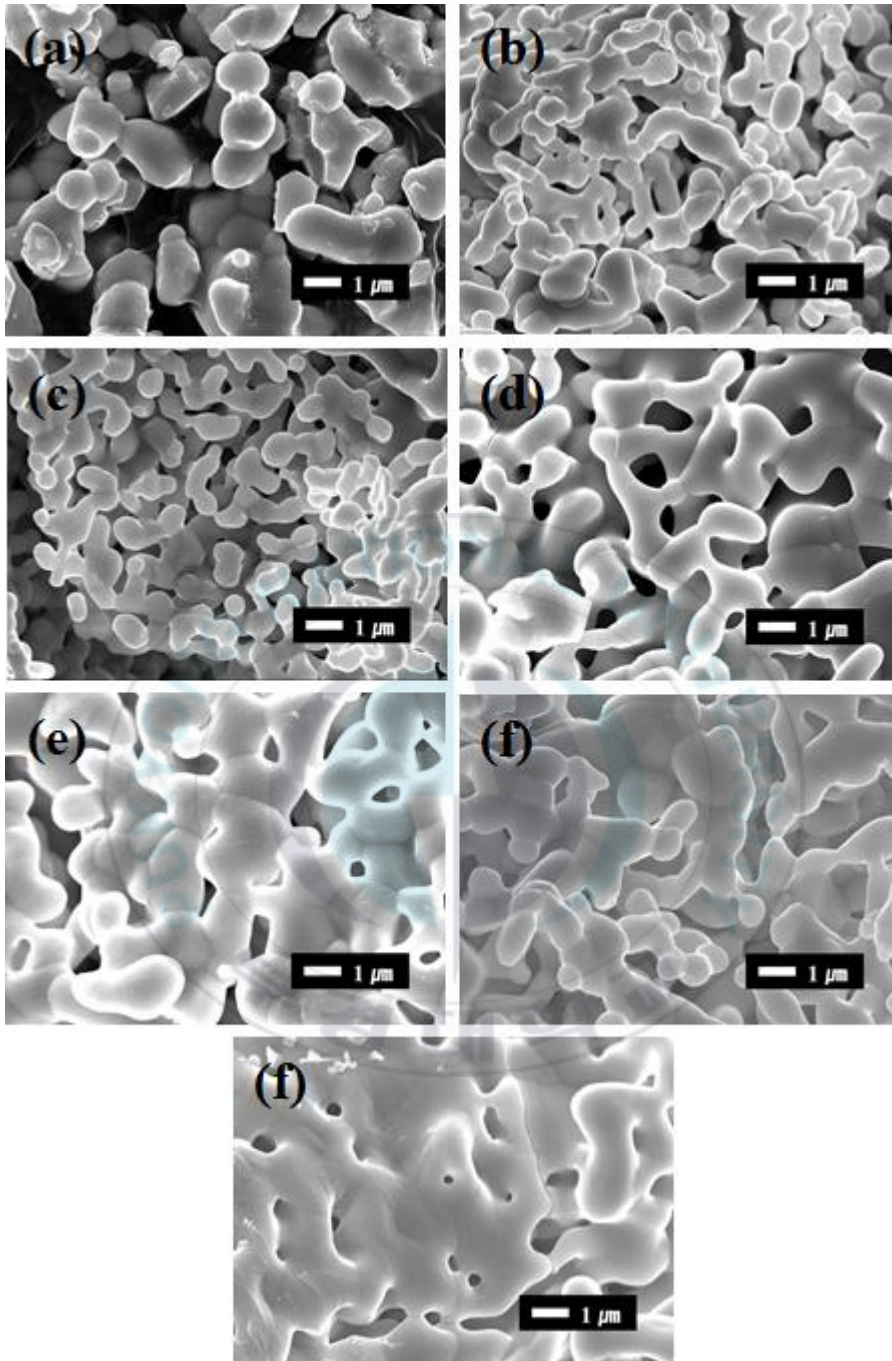


Figure 4. 17 FE-SEM images of $Gd_{0.95}Ce_{0.05}Sr_2AlO_5:xLi^+$ where (a) $x = 0$, (b) $x = 0.025$, (c) $x = 0.050$, (d) $x = 0.100$, (e) $x = 0.150$, (f) $x = 0.200$ and (g) $x = 0.250$.

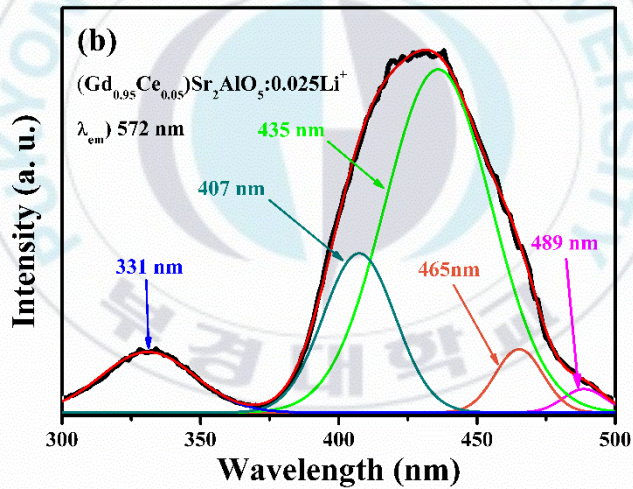
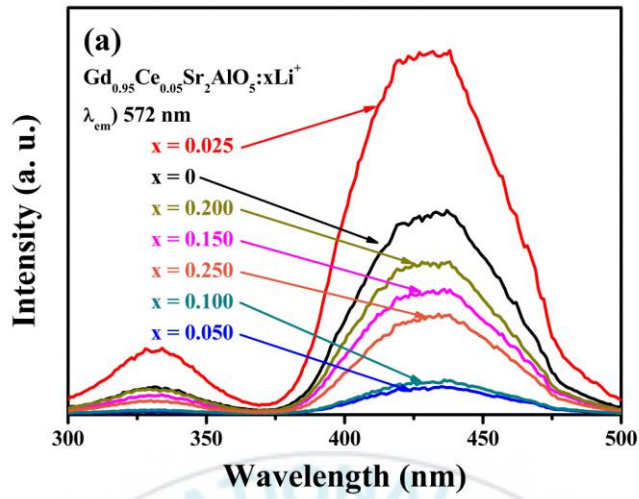
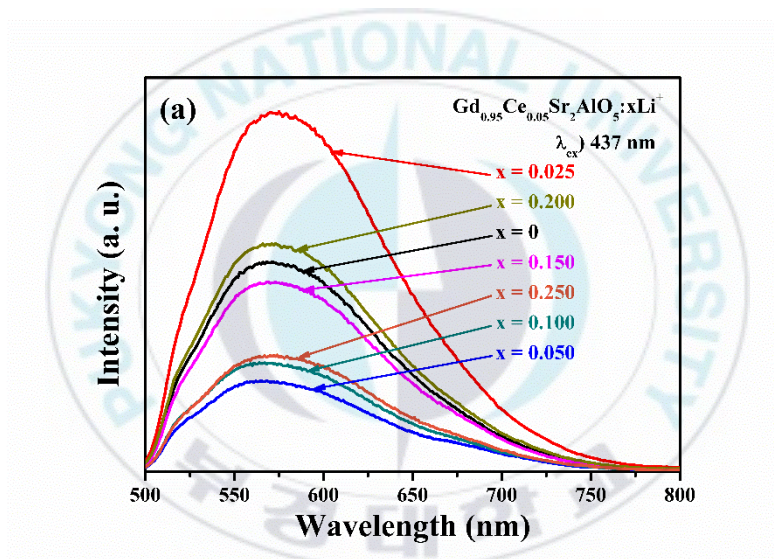


Figure 4. 18 (a) PLE spectra ($\lambda_{em} = 572$ nm) and (b) Gaussian function fitting graph of PLE spectra for $Gd_{0.95}Ce_{0.05}Sr_2AlO_5:0.025Li^+$ phosphor.

Figure 4. 18 displays the (a) PLE spectra and (b) Gaussian function fitting graph of PL spectra for $Gd_{0.95}Ce_{0.05}Sr_2AlO_5:0.025Li^+$ phosphor. The PLE

spectra has a weak excitation region ranging from 300 nm to 375 nm and a dominant excitation band between 375 nm and 500 nm due to the 4f-5d transition of Ce^{3+} . The computed wavelength corresponding with the 4f-5d transition energy of the Ce^{3+} ion are 331 nm, 407 nm, 435 nm, 465 nm and 489 nm. The excitation spectra and fitted Gaussian peaks were not shifted for different Li^+ concentration. The calculated crystal splitting energy of GSA: Ce^{3+} , Li^+ phosphors was 10000 cm^{-1} .



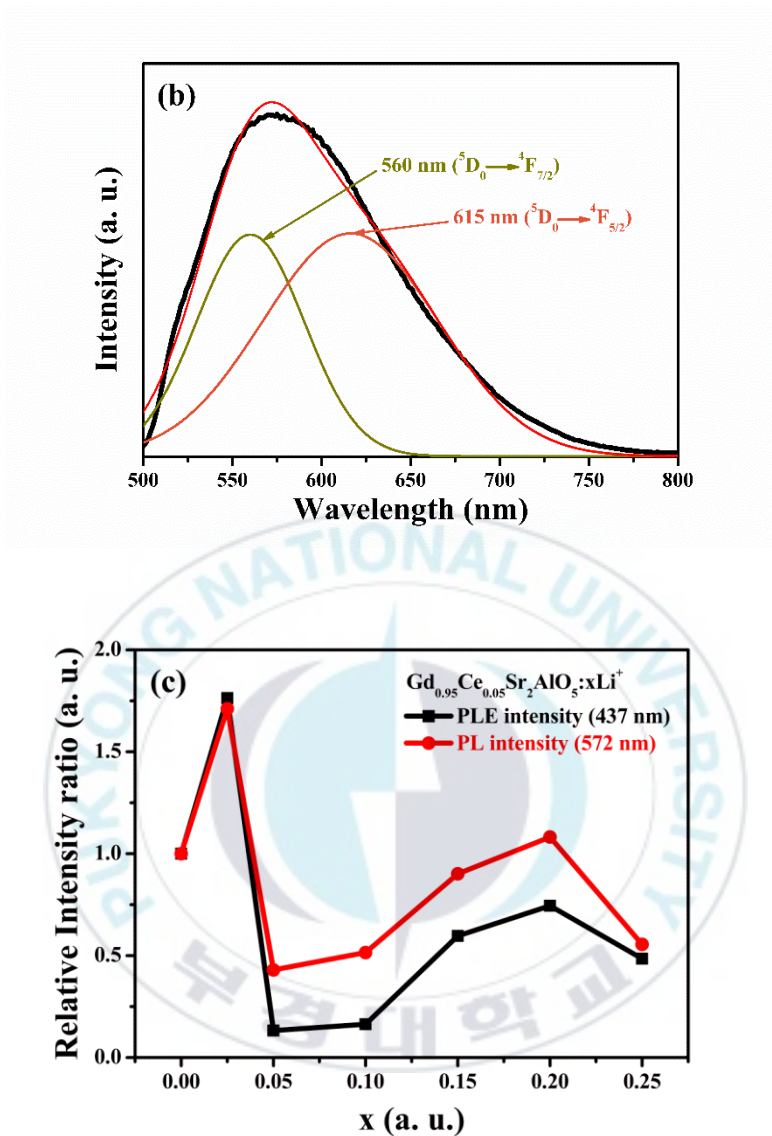


Figure 4. 19 (a) PL spectra ($\lambda_{\text{ex}} = 437 \text{ nm}$), (b) Gaussian function fitting graph of PL spectra and (c) PL, PLE intensity graph of GSA:Ce³⁺, Li⁺ phosphors as a function of Li⁺ concentration.

Figure 4. 18 displays the (a) PL spectra, (b) Gaussian function fitting

graph of PL spectra and (c) PL, PLE intensity graph of GSA:Ce³⁺, Li⁺ phosphors as a function of Li⁺ concentration. The PL spectra exhibits the maximum intensity at 572 nm and a broad emission band ranging from 475 nm to 750 nm because of the 5d-4f transition of Ce³⁺. The dominant excitation and emission wavelengths were not moved by increasing the Li⁺ concentration in GSA:Ce³⁺, Li⁺ phosphors. The emission spectra of GSA:Ce³⁺, Li⁺ phosphors were computed to the sum of two Gaussian peaks centered at 560 nm and 615 nm corresponding to the 5d-4f transition energy of Ce³⁺. The 5d-4f transition energy of Ce³⁺ in GSA:Ce³⁺, Li⁺ were not changed by increasing the Li⁺ contents of GSA:Ce³⁺, Li⁺ phosphors. However, Since x was 0.025, the excitation and emission intensity was enhanced to 1.7 times in comparison with GSA:Ce³⁺ phosphors (x = 0). The substitution of Li⁺ ion into the GSA:Ce³⁺ host lattice can give local distortion of the host lattice that can optimizing the environment around the Ce³⁺ ions [32]. The emission and excitation intensity was quenched to further Li⁺ concentration. The emission intensity and excitation intensity changed when the x value increase from 0.100 to x = 0.250 due to the particle size and morphology of the GSA:Ce³⁺, Li⁺ phosphors. In general, the growth of particle size enhance the excitation and emission intensity due to the increase of excitation area and scattering. The aggregation of phosphor particles can decrease the prevent of the light scattering and

output emission intensity.

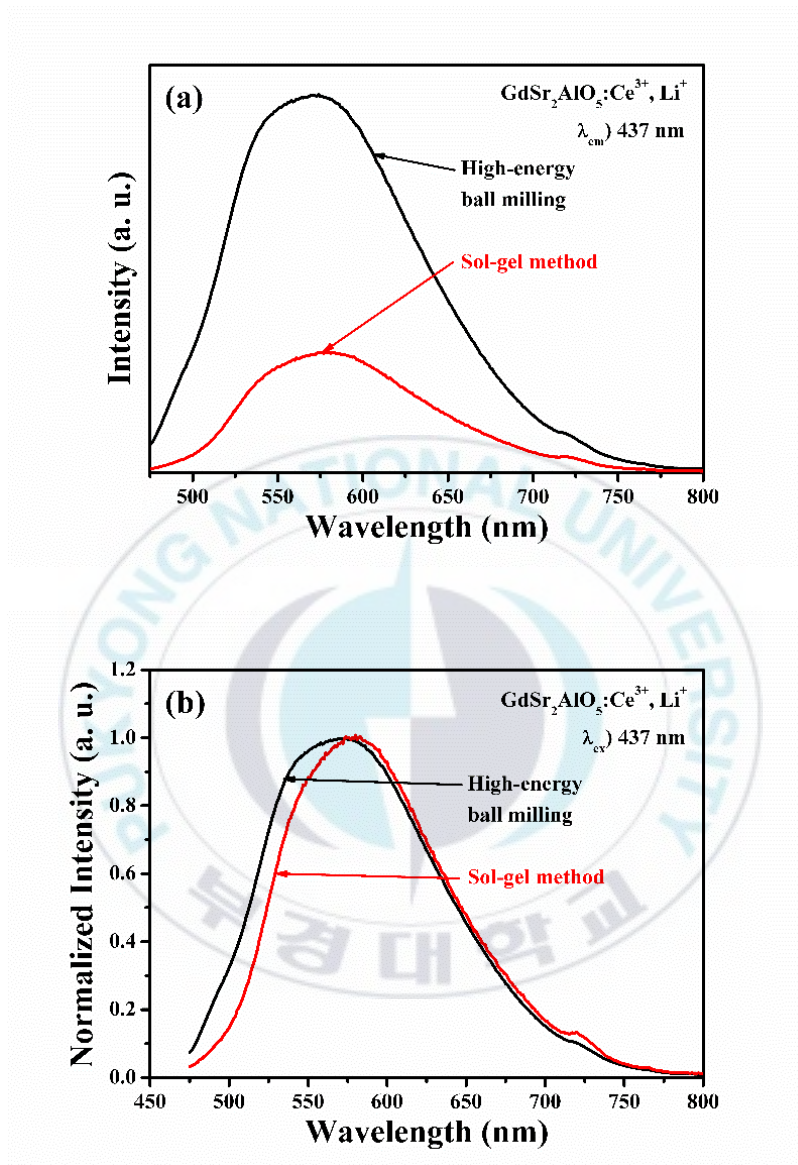


Figure 4. 20 Comparison of (a) PL spectra and (b) normalized PL spectra of $\text{GSA}:\text{Ce}^{3+}, \text{Li}^+$ phosphor synthesized by high-energy ball milling and sol-gel method.

The Comparison of PL spectra and normalized PL spectra of $\text{GSA}:\text{Ce}^{3+}$,

Li^+ phosphor for different synthesis method were shown in Figure 4. 19. For sol-gel method, the PL intensity of $\text{GSA}:\text{Ce}^{3+}$, Li^+ phosphors was 3 times lower, since the difference of the particle size and morphology. However, the PL intensity of the $\text{GSA}:\text{Ce}^{3+}$, Li^+ phosphors, exhibits better color purity due to the low quantity of impurity(GdSrAlO_4 phase) in comparison with high-energy ball milling method.

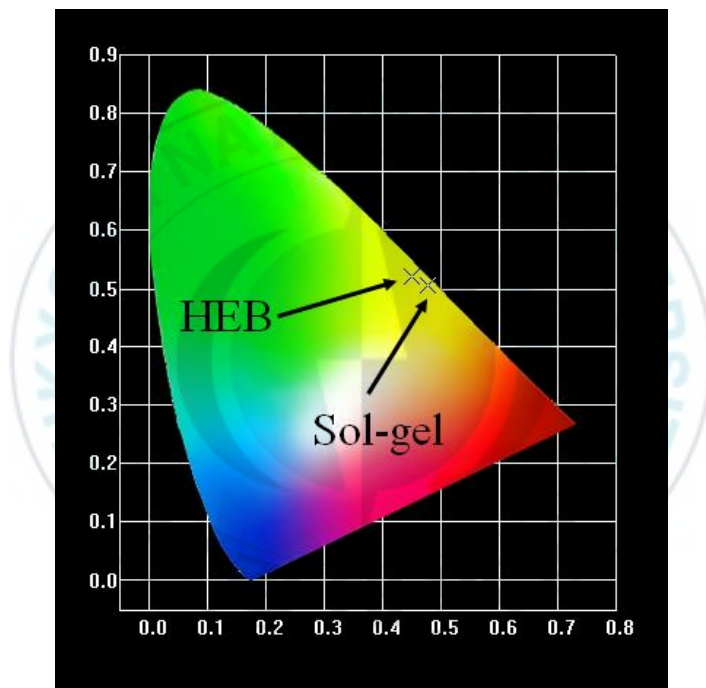


Figure 4. 21 CIE color coordinate of $\text{GSA}:\text{Ce}^{3+}$, Li^+ phosphor synthesized by high-energy ball milling (HEB) and sol-gel method.

Figure 4. 20 depicts the CIE color coordinate of $\text{GSA}:\text{Ce}^{3+}$, Li^+ phosphors synthesized by high-energy ball milling and sol-gel method. The calculated color coordinate of $\text{GSA}:\text{Ce}^{3+}$, Li^+ phosphors fabricated by high-

energy ball milling and sol-gel method were (0.478, 0.506), (0.451, 0.520), respectively. The color coordinate of the phosphors synthesized by sol-gel method shifted to yellow region due to the decline of the green emission.



5. Conclusion

GSA:Ce³⁺ yellow phosphors were prepared by the high-energy ball milling process. The crystal structure, surface morphology and luminescence properties and white LED performance were investigated for different Ce³⁺ concentration. The X-ray diffraction pattern confirmed that the synthesized phosphors consisted of GdSr₂AlO₅ phase and GdSrAlO₄ impurity phase. The surface morphology of GSA:Ce³⁺ shows that 5 μm size of irregular shaped particles, which were aggregated regardless of the Ce³⁺ concentration. The photoluminescence excitation spectra shown the dominant excitation band at around 438 nm due to the 4f-5d transition of Ce³⁺ ion. The photoluminescence emission spectra exhibited broad yellow emission band due to the 5d-4f transition of the Ce³⁺ ion in GSA host lattice. As the Ce³⁺ ion doped to 2 mol% in GSA:Ce³⁺ phosphors, the emission intensity at 576 nm (dominant wavelength) reaches to its maximum value. The 5d-4f transition energy of GSA:Ce³⁺ phosphor were shifted to a red region by doping higher Ce³⁺ concentration. The CIE 1931 chromaticity coordinates of the white LEDs combined with the blue LED chips (460 nm) and the Gd_{0.98}Ce_{0.02}Sr₂AlO₅ yellow phosphors were (0.347, 0.311). For these results, the GSA:Ce³⁺ phosphors can be used as yellow phosphor in warm white LEDs.

The GSA:Ce³⁺, Li⁺ phosphors were synthesized by using a high-energy ball milling method for different Li⁺ concentration. The XRD patterns confirmed their tetragonal structure with a poly crystalline GdSr₂AlO₅ phase and GdSrAlO₄ phase. The Li⁺ co-doping affected the relative intensity of XRD peaks in GdSr₂AlO₅ phase. The SEM images showed irregular shape in the size of 10 μm irrespective of the Li⁺ concentration.

The most dominant excitation band between 375 and 500 nm has the highest value at 437 nm regardless of the Li⁺ concentration. The GSA:Ce³⁺, Li⁺ phosphors have a broad yellow emission band centered at 574 nm due to the 5d-4f transition of Ce³⁺. The yellow emission of GSA:Ce³⁺ was enhanced by a factor of 5.17 by adding 10 mol% of Li⁺ in comparison with Li⁺ un-doped GSA:Ce³⁺ phosphor. The mechanism of the luminescence enhancement is essentially regarded as the result of crystal field distortion around Ce³⁺ ion by co-doping Li⁺ ions. The enhancement of the yellow emission in GSA:Ce³⁺, Li⁺ phosphors displayed color rendering improvement of white LEDs. Applying GSA:Ce³⁺, Li⁺ in white LEDs permits better color rendering (R_a = 83, CCT = 4333K) than GSA:Ce³⁺ encapsulated white LEDs (R_a = 78, CCT = 10281K).

The GSA:Ce³⁺, Li⁺ phosphors were synthesized by using sol-gel method for different Li⁺ concentration. The XRD patterns confirmed their tetragonal structure with a poly crystalline GdSr₂AlO₅ phase and GdSrAlO₄

impurity phase. Using a sol-gel method, the crystallinity of the impurity phase decreased in comparison of the high-energy ball milling. Increasing the Li^+ concentration of GSA:Ce^{3+} , Li^+ phosphors promoted the particle grow and aggregation each other. The GSA:Ce^{3+} , Li^+ phosphors have dominant emission wavelength at 572 nm with 437 nm excitation. When the Li^+ concentration in GSA:Ce^{3+} , Li^+ was 2.5 mol%, the emission intensity of GSA:Ce^{3+} was increased by an enhancement factor of 1.7. Those from sol-gel method give rise to low emission intensity and high color purity due to the difference of morphology and impurity contents.

Hence, the GSA:Ce^{3+} phosphors can be used for InGaN-based white LEDs. Optimizing the synthesis condition and co-doping Li^+ could promote the color purity and the luminescence intensity of GSA:Ce^{3+} phosphors.

Reference

- [1] M. B. Krames, O. B. Shchekin, R. Mueller-Mach, G. O. Mueller, L. Zhou, G. Harbers and M. G. Craford, *J. Display Technol.*, 2007, 3, 2, 160.
- [2] N. Narendran, Y. Gu, J. P. Freyssinier, H. Yu and Deng. L, *J. Cryst. Growth*, 2004, 268, 3–4, 449.
- [3] AK. Pachur, AI. Prasad, AA. Ansari, SB. Rai and RS. Ningthoujam, *Dalton Trans.*, 2012, 41, 36, 11032.
- [4] J. Y. Park, H. C. Jung, G. S. R. Rasu, B. K. Moon, J. H. Jeong and J. H. Kim, *Solid State Sci.*, 2010, 12, 5, 719.
- [5] E. F. Schubert and J. K. Kim, *Science*, 2005, 308, 5726, 1274-1278.
- [6] S. Ye, F. Xiao, YX. Pan, YY. Ma and QY. Zhang, *Mater. Sci. Eng. R-Rep.*, 2010, 71, 1, 1.
- [7] G. Blasse and A. Bril, *Appl. Phys. Lett.*, 1967, 11, 2, 53.
- [8] D. Chen and Y. Chen, *Ceram. Int.*, 2014, 40, 9, Part B, 15325.
- [9] S. Nishiura, S. Tanabe, K. Fujioka and Y. Fujimoto, *Opt. Mater.*, 2011, 33, 5, 688.
- [10] HS. Jang, Y-H. Won and DY. Jeon, *Appl. Phys. B*, 2009, 95, 4, 715.
- [11] Q. Li, G. Lian and D. Yan, *Mater. Chem. Phys.*, 2000, 64, 1, 41.
- [12] H. Liu, Y. Luo, Z. Mao, L. Liao and Z. Xia, *J. Mater. Chem. C*, 2014,

- 2, 9, 1619.
- [13] T. Nishida, T. Ban and N. Kobayashi, *Appl. Phys. Lett.*, 2003, 82, 22, 3817.
- [14] M. Jiao, W. Lv, W. Lv, Q. Zhao, B. Shao and H. You, *Dalton Trans.*, 2015, 44, 4080.
- [15] J-U. Kim, Y-S. Kim and H. Yang, *Mater. Lett.*, 2009, 63, 6–7, 614-616.
- [16] M. Yamada, T. Naitou, K. Izuno, H. Tamaki, Y. Murazaki, M. Kameshima and T. Mukai, *Jpn. J. Appl. Phys.*, 2003, 42, L20.
- [17] H. S. Jang, W. B. Im, D. C. Lee, D. Y. Jeon and S. S. Kim, *J. Lumin.*, 2007, 126, 2, 371.
- [18] X. Li, J. D. Budai, F. Liu, J. Y. Howe, J. Zhang, X-J. Wang, Z. Gu, C. Sun, R. S. Meltzer and Z. Pan, *Light Sci. Appl.*, 2013, 2, 1, e50.
- [19] Y-C. Wu, Y-C. Chen, T-M. Chen, C-S. Lee, K-J. Chen and H-C. Kuo, *J. Mater. Chem.*, 2012, 22, 16, 8048.
- [20] XM. Wang, X. Zhang, S. Ye and XP. Jing, *Dalton Trans.*, 2013, 42, 14, 5167.
- [21] X. Min, M. Fang, Z. Huang, Y. Liu, C. Tang and X. Wu, *Ceram. Int.*, 2015, 41, 3, Part A, 4238.
- [22] J. Y. Park, J. H. Lee, G. S. R. Rasu, B. K. Moon, J. H. Jeong, B. C. Choi and J. H. Kim, *Ceram. Int.*, 2014, 40, 4, 5693.
- [23] W. B. Im, Y. Fourré, S. Brinkley, J. Sonoda, S. Nakamura, S. P.

- DenBaars and R. Seshadri, *Opt. Express*, 2009, 17, 25, 22673.
- [24] W. B. Im, N. N. Fellows, S. P. DenBaars and R. Seshadri, *J. Mater. Chem.*, 2009, 19, 9, 1325.
- [25] W. B. Im, N. N. Fellows, S. P. DenBaars, R. Seshadri and Y-I. Kim, *Chem. Mater.*, 2009, 21, 13, 2957.
- [26] J. H. Kim and K. Y. Jung, *J. Lumin.*, 2012, 132, 6, 1376-1381
- [27] J. Liu, J. Sun and C. Shi, *Mater. Lett.*, 2006, 60, 2830.
- [28] Y. Kojima, K. Aoyagi and T. Yasue, *J. Lumin.*, 2005, 115, 13.
- [29] L. Chen, Y. Zhang, F. Liu, A. Luo, Z. Chen, Y. Jiang, S. Chen and R. S. Liu, *Mater. Res. Bull.*, 2012, 47, 4071.
- [30] X. Wang, J. Li, Q. Shen and P. Shi, *Ceram. Int.*, 2014, 40, 9, Part B, 15313.
- [31] K. Dong, Z. Li, S. Xiao, Z. Xiang, X. Zhang, X. Yang and X. Jin, *J. Alloys Compd.*, 2012, 543, 105.
- [32] L. Jia, M. Gu, X. Liu, S. Huang, B. Liu and C. Ni, *IEEE Trans. Nucl. Sci.*, 2010, 57, 1268.
- [33] Z. Hao, X. Zhang, Y. Luo, L. Zhang, H. Zhao and J. Zhang, *J. Lumin.*, 2013, 140, 78.
- [34] W. B. Im, K. Page, S. P. DenBaars and R. Seshadri, *J. Mater. Chem.*, 2009, 19, 46, 8761.
- [35] L. Van Pieterson, M. F. Reid, R. T. Wegh, S. Soverna, and A. Meijerink,

- Phys. Rev. B, 2002, 65, 045113
- [36] S. Shionoya and W. M. Yen, Phosphor Handbook, CRC press Boston, 1999.
- [37] S. Tanabe, S. Fujita, S. Yoshihara, A. Sakamoto and S. Yamamoto, Proc. Of SPIE., 2005, 594112
- [38] L. S. Dent, F. P. Glasser, Acta Crystallogr. 1965, 18, 453.
- [39] L. G. Van Uitert, J. Lumin., 1984, 29, 1
- [40] B. K. Grandhe, V. R. Bandi, K. Jang, H. S. Lee, D. S. Shin, S. S. Yi and J. H. Jeong, Ceram. Int., 2012, 38, 6273.
- [41] C. Shen, K. Li and Y. Yang, Proc. SPIE, 2009, 7635, 76350K.
- [42] H. K. Yang and J. H. Jeong, J. Phys. Chem. C, 2009, 114, 226.
- [43] HJ. Fecht, E. Hellstern, Z. Fu and WL. Johnson, Metall. Trans. A, 1990, 21, 2333.
- [44] G. Blasse, J. Solid State Chem., 1986, 62, 207.
- [45] P. D. Rack and P. H. Holloway, Mater. Sci. Eng. R, 1998, 21, 171.
- [46] H. S. Jang, W. B. Im, D. C. Lee, D. Y. Jeon and S. S. Kim, J. Lumin., 2007, 126, 371.